Structural and functional insights into the activation of the dual incision activity of UvrC, a key player in bacterial NER

Anna Seck, Salvatore de Bonis, Meike Stelter, Mats Ökvist, Müge Senarisoy, Mohammad Rida Hayek, Aline Le Roy, Lydie Martin, Christine Saint-Pierre, Célia M Silveira, et al.

To cite this version:

Anna Seck, Salvatore de Bonis, Meike Stelter, Mats Ökvist, Müge Senarisoy, et al.. Structural and functional insights into the activation of the dual incision activity of UvrC, a key player in bacterial NER. Nucleic Acids Research, 2023, 51 (6), pp.2931-2949. 10.1093/nar/gkad108 . hal-04099160

HAL Id: hal-04099160

https://hal.science/hal-04099160

Submitted on 16 Nov 2023

Nucleic Acids Research, 2023, Vol. 51, No. 6 **2931–2949**
https://doi.org/10.1093/nar/gkad108

Structural and functional insights into the activation of the dual incision activity of UvrC, a key player in bacterial NER

Anna Seck[1,2,†], Salvatore De Bonis[1,†], Meike Stelter[1,3], Mats Ökvist[3], Müge Senarisoy[1], Mohammad Rida Hayek[1], Aline Le Roy[1], Lydie Martin[1], Christine Saint-Pierre[2], Célia M. Silveira[4], Didier Gasparutto[2], Smilja Todorovic[4], Jean-Luc Ravanat[2] and Joanna Timmins[1,*]

[1]Univ. Grenoble Alpes, CEA, CNRS, IBS, F-38000 Grenoble, France, [2]Univ. Grenoble Alpes, CEA, CNRS, SyMMES-UMR 5819, F-38000 Grenoble, France, [3]European Synchrotron Radiation Facility, F-38000 Grenoble, France and [4]Instituto de Tecnologia Química e Biológica António Xavier, Universidade NOVA de Lisboa, Av. da República, 2780-157 Oeiras, Portugal

Received September 28, 2022; Revised January 10, 2023; Editorial Decision February 03, 2023; Accepted February 06, 2023

ABSTRACT

Bacterial nucleotide excision repair (NER), mediated by the UvrA, UvrB and UvrC proteins is a multistep, ATP-dependent process, that is responsible for the removal of a very wide range of chemically and structurally diverse DNA lesions. DNA damage removal is performed by UvrC, an enzyme possessing a dual endonuclease activity, capable of incising the DNA on either side of the damaged site to release a short single-stranded DNA fragment containing the lesion. Using biochemical and biophysical approaches, we have probed the oligomeric state, UvrB- and DNA-binding abilities and incision activities of wild-type and mutant constructs of UvrC from the radiation resistant bacterium, *Deinococcus radiodurans*. Moreover, by combining the power of new structure prediction algorithms and experimental crystallographic data, we have assembled the first model of a complete UvrC, revealing several unexpected structural motifs and in particular, a central inactive RNase H domain acting as a platform for the surrounding domains. In this configuration, UvrC is maintained in a 'closed' inactive state that needs to undergo a major rearrangement to adopt an 'open' active state capable of performing the dual incision reaction. Taken together, this study provides important insight into the mechanism of recruitment and activation of UvrC during NER.

INTRODUCTION

Nucleotide excision repair (NER) is a conserved and versatile DNA repair pathway found in all domains of life (1–3). It is responsible for the removal of a very wide range of chemically and structurally diverse DNA lesions. This includes adducts caused by smoking or generated by chemotherapy and UV-induced lesions such as pyrimidine-pyrimidone (6–4) photoproducts (6–4-PP) and cyclobutane pyrimidine dimers (CPD), all of which are proposed to distort or destabilize the DNA duplex to some extent. In prokaryotes, NER is mediated by the UvrA, UvrB and UvrC proteins in a multistep, ATP-dependent process (1–3). UvrA, acting as a dimer, and possibly with the help of UvrB, is responsible for DNA damage recognition (4–6). UvrA alone has been shown to bind preferentially to damaged DNA (7–9). UvrA proteins consist of two tandemly arranged ATP-binding cassette-like nucleotide-binding domains (9–11) and the crystal structure of *T. thermophilus* UvrA in complex with fluorescein-adducted DNA suggests that UvrA recognizes the distortion in the DNA duplex, rather than the DNA lesion itself (12). In addition to its role in damage localization, UvrA is also responsible for recruiting UvrB to sites of DNA damage (4,13,14), although the exact details of this process are still unclear. Single-molecule studies using DNA tightropes and quantum-dot labelled proteins have shown that association of UvrB with UvrA significantly increases the efficiency with which DNA lesions are located (15), while in *E. coli*, single-molecule localization imaging has revealed that UvrA scans the genome alone to locate DNA lesions and then recruits UvrB to the damaged site (13).

---

[*] To whom correspondence should be addressed. Tel: +33 4 57 42 86 78; Email: joanna.timmins@ibs.fr

[†] The authors wish it to be known that, in their opinion, the first two authors should be regarded as Joint First Authors.

Present address: Mats Ökvist, Norwegian Medicines Agency, Oslo, Norway.

UvrB plays a central role in bacterial NER (1–3); it interacts with the damaged DNA and the two other Uvr proteins. UvrB is structurally well-characterized and structures of UvrB in both its apo- and DNA-bound form have been solved (16–20). UvrB possesses a weak helicase and ATPase activity which is only activated after interaction with UvrA to allow UvrB to locally unwind the DNA duplex and stably associate with the lesion-containing strand (4). The oligomeric state of UvrB is controversial with some studies indicating that it is monomeric and others that it functions as a dimer (21), similar to UvrA. There is, however, increasing data supporting the hypothesis that UvrA and UvrB may function together as a complex composed of a UvrA dimer associated with two UvrB monomers, which would be loaded onto the DNA up to 80 Å away from the DNA lesion (4,6,15,22). Once loaded onto the DNA, UvrB plays a decisive role in discriminating between damaged and intact DNA. This verification process involves a conserved β-hairpin motif that has been shown to insert itself between the two strands of the damaged DNA, causing the damaged base to be flipped out into a hydrophobic pocket of UvrB (4,16,19). The stable binding of UvrB to the damaged DNA to form the pre-incision complex triggers the release of UvrA and subsequently ensures a precise incision by UvrC to release a 12 to 13 nucleotide DNA fragment containing the damaged base (1–3).

UvrC is an enzyme possessing a dual endonuclease activity catalyzed by two independent endonuclease domains: one located at its N-terminus that is responsible for the 3′ incision and another located at its C-terminus that is in charge of the 5′ incision (1–3,23–26). *Mycobacterium tuberculosis* UvrC (MtUvrC) has additionally been shown to possess an intrinsic DNA-independent ATPase activity (27). Crystal structures of the two catalytic domains of *Thermatoga maritima* UvrC (TmUvrC) have been determined. The N-terminal endonuclease domain (NEndo) is composed of the first 90–100 amino acids of UvrC (Figure 1A) and shares sequence and structural homology with the catalytic domains of members of the GIY-YIG endonuclease superfamily, while the C-terminal endonuclease domain shares structural homology with members of the RNase H family of enzymes (25,26). In *Escherichia coli*, *T. maritima* and *Bacillus caldotenax*, the NEndo domain has been shown to catalyze the first incision reaction on the 3′ side of the damaged nucleotide, an activity that requires a divalent cation (magnesium or manganese) and the presence of either UvrB or the double helix-hairpin-helix $(HhH)_2$ motif located at the C-terminal end of UvrC (Figure 1A) (28,29). This first incision then enables the C-terminal RNase H domain to perform the second incision reaction on the 5′ side of the lesion. This step also requires a divalent cation and a conserved DDH triad motif. Here again, efficient cleavage requires the presence of the C-terminal $(HhH)_2$ DNA binding motif (28). Dual $(HhH)_2$ motifs are commonly found in non-specific DNA-binding proteins, where they have been found to interact with the phosphate backbone of the DNA minor groove (30,31). In TmUvrC, the $(HhH)_2$ motif is linked via a flexible linker to the RNase H domain (26) and shows structural and sequence similarity with the $(HhH)_2$ domains of ERCC1, which together with XPF, form the endonuclease complex responsible for 5′ incision in mammalian NER (32). As in the ERCC1/XPF complex, the $(HhH)_2$ motif of UvrC can bind ssDNA-dsDNA junctions (28).

The central region of UvrC stretching between the N-terminal GIY-YIG endonuclease domain and the C-terminal RNase H domain, for which no structural information is available, harbors a cysteine-rich motif that has recently been proposed to coordinate a [4Fe–4S] cluster needed for DNA-mediated charge transfer chemistry (33) and the UvrB interaction site (Figure 1A). Little is known regarding the nature of the complex formed between UvrB and UvrC. The use of single-molecule studies and DNA tightropes have shown that *B. caldotenax* UvrB and UvrC can form a tight complex on DNA and that binding of UvrC to UvrB alters the DNA binding properties of UvrB, suggesting that a UvrB–UvrC complex may form prior to DNA binding (34). The UvrB-interacting region of UvrC has been shown to interact with UvrB's C-terminal domain, with which it shares homology. The latter forms a helix-loop-helix fold, which is capable of dimerizing. The homologous region in UvrC has thus been proposed to adopt the same fold allowing it to hetero-dimerize with the equivalent UvrB domain (35,36). In *E. coli* UvrC, this interaction is required for 3′ incision, but not for 5′ incision (37,38).

Bacterial NER has been successfully reconstituted *in vitro* using the three essential UvrA, UvrB and UvrC proteins from either *E. coli* (39–41) or more recently from thermophilic bacteria (*B. caldotenax*, *Geobacillus stearothermophilus, T. maritima* and *T. thermophilus*) (4,15,25,26,34,42,43), and either lesion-containing plasmid or DNA oligonucleotides as substrates (39–42,44). We recently developed a highly efficient incision assay (45) relying on the activity of UvrA, UvrB and UvrC from a single organism, the mesophilic and radiation resistant bacterium, *Deinococcus radiodurans* that possesses a well-conserved NER system (46). In the present study, we have used this assay, together with biochemical, mutational, biophysical and structural studies, to (i) unveil the nature and particularities of the FeS cluster of *D. radiodurans* UvrC (DrUvrC), (ii) provide important insight into the regulation and coupling of the incision activities of DrUvrC, (iii) identify a remarkable feature of the N-terminal region of DrUvrC that is capable of catalyzing the dual incision reaction in the absence of the C-terminal endonuclease domain of UvrC, and (iv) establish the first complete three-dimensional model of a UvrC protein and propose a model of DNA-bound UvrC.

MATERIALS AND METHODS

Cloning, expression and purification of uvr proteins

Cloning, expression and purification of *D. radiodurans* UvrA1 (DR_1771), UvrB (DR_2275) and UvrC (DR_1354) have been described previously (45). Truncated constructs (Table S1) of UvrC (DR_1354) were cloned into pProex-HtB (EMBL) for expression with a cleavable N-terminal His-tag. A construct corresponding to residues 94 to 366 was also prepared, but could not be expressed in a soluble form, indicating that the presence of the well-folded NEndo domain is required for proper folding of the central region bearing the Cys-rich motif and the UvrB binding motif. UvrC mutants ($UvrC^{E72A}$, $UvrC^{D391A}$, $UvrC\text{-}N^{E72A}$ and $UvrC\text{-}C^{D391A}$) were prepared with primers listed

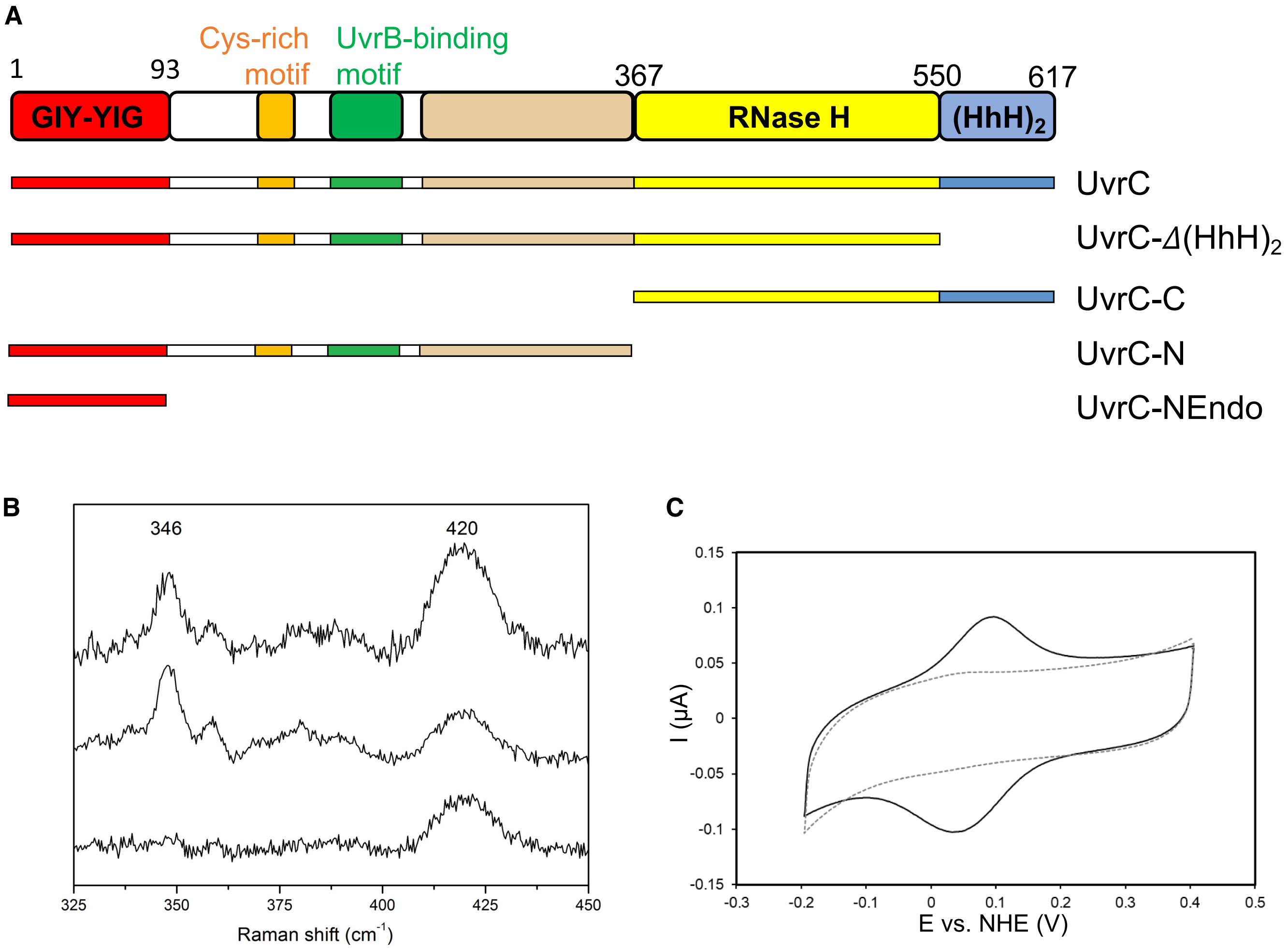

Figure 1. Primary structure and domain organization of UvrC and characterization of its FeS cluster. (**A**) Schematic diagram of UvrC and its known domains and functional motifs. At the start of this study, little was known regarding the central domain (beige). The different constructs used in this study (UvrC, UvrC-Δ(HhH)$_2$, UvrC-C, UvrC-N and UvrC-NEndo) are illustrated below. (**B**) Resonance Raman spectra of anaerobically purified DrUvrC (top trace), aerobically purified DrUvrC (middle trace) and the buffer (lower trace), measured with 406 nm excitation. Vibrational mode at 346 cm^{-1} is characteristic of [3Fe–4S]$^{1+}$ cluster; the band at 420 cm^{-1}, present also in the buffer, originates from glycerol. (**C**) Cyclic voltammograms of SAM-coated Au electrode before (dotted trace) and after immobilization of DrUvrC (solid trace). Measurements were performed in 50 mM Tris–HCl pH 7.5 and 100 mM NaCl at a scan rate of 50 mV s^{-1}.

in Table S2 as described previously (47). All constructs were expressed in *E. coli* BL21 cells and expression was induced at 20°C overnight with 1 mM isopropyl- β-D-thiogalactopyranoside (IPTG). UvrC-Δ(HhH)$_2$, UvrC^{E72A} and UvrC^{D391A} were purified as for UvrC wild-type (45). For the anaerobic purification of UvrC, all steps (from cell lysis to protein freezing at –80°C for long-term storage) were performed in a glovebox with oxygen levels below 5 ppm. The purification protocol was adjusted for the purification of UvrC-NEndo, UvrC-N and UvrC-C and their respective point mutants. For these constructs, cell pellets were lysed in buffer A1 composed of 50 mM Tris–HCl pH 7.0 (UvrC-NEndo) or 8.0 (UvrC-N and UvrC-C), 1 M NaCl, 10% glycerol, 1 mM MgCl$_2$ and 2 mM beta-mercaptoethanol (β-ME), supplemented with protease inhibitors (Roche). DNase I, lysozyme (Roche) and S7 nuclease were added to the cell suspension prior to lysis by sonication. Cleared cell lysates were loaded on a 5 ml HisTrap FF column (GE Healthcare) equilibrated in buffer A1, after which the column was washed with buffer A1 supplemented with 25 mM (UvrC-C) or 50 mM (UvrC-NEndo and UvrC-N) imidazole and the protein was eluted with buffer A1 supplemented with 250 mM imidazole (UvrC-NEndo and UvrC-N) or with buffer A2 composed of 50 mM Tris–HCl pH 8.0, 0.2 M NaCl, 2.5 mM MgCl$_2$, and 50 mM imidazole. UvrC-N and UvrC-NEndo were then further purified by size-exclusion chromatography (SEC) on SEC650 (UvrC-N; Bio-Rad) or SEC70 (UvrC-NEndo; Bio-Rad) columns equilibrated in buffer A1. The fractions containing the protein were pooled and digested with TEV protease (1:20 w/w ratio) at 4˚C overnight. For UvrC-C, the protein eluted from the HisTrap column was directly digested with TEV protease (1:20 w/w ratio) at 4˚C overnight. In all cases, uncleaved UvrC and the His-tagged TEV protease were removed by performing a second Nickel affinity column using 1 ml Ni-sepharose resin (Macherey-Nagel). The cleaved proteins were recovered in the flow-through and were subjected to a final SEC purification on SEC650 (UvrC-N and

UvrC-C) or SEC70 (UvrC-NEndo) columns equilibrated in 50 mM Tris–HCl pH 8, 500 mM NaCl, 10% glycerol, 1 mM $MgCl_2$, 2 mM β-ME (UvrC-NEndo and UvrC-N) or 50 mM Tris–HCl pH 8 and 200 mM NaCl. All proteins were stored at -80°C and were diluted in 50 mM Tris–HCl pH 8.0, 150 mM NaCl, 5% glycerol and 2 mM β-ME prior to use in the incision assay.

Size-exclusion chromatography (SEC) and SEC-multi-angle laser light scattering (MALLS)

20 μM UvrB was mixed with either 25 μM UvrA1 or 25 μM UvrC (wild-type and truncated constructs; Table S1) in binding buffer composed of 50 mM Tris–HCl pH 8.0, 300 mM NaCl, 5% glycerol and 2 mM β-ME and after 15 min incubation at room temperature, the mixes were separated by SEC on a SEC650 column (Bio-Rad) equilibrated in binding buffer. Elution fractions were analyzed on TGX stain-free SDS-PAGE gels (Bio-Rad) allowing the protein bands to be visualized directly after migration on a Chemidoc MP imager (Bio-Rad). The oligomeric states of UvrC, UvrC-Δ(HhH)$_2$, UvrC-NEndo and UvrC-C were analyzed by SEC coupled to multi-angle laser light scattering (MALLS), dynamic light scattering (DLS) and refractometry (RI). SEC-MALLS experiments were performed with a Superdex 200 10/300 GL column equilibrated with either 50 mM Tris pH 8.0, 300 mM NaCl, 5% glycerol and 5 mM β-ME or 50 mM Tris pH 8.0, 1 M NaCl, 5% glycerol and 5 mM β-ME. 20 μl protein solution at 2–10 mg ml^{-1} was injected onto the column at 0.5 ml min^{-1}. On-line MALLS detection was performed with a miniDAWN-TREOS detector (Wyatt), DLS was recorded with a DynaPro Nanostar and RI measurements were performed with an Optilab eEX system (Wyatt).

Bacterial two-hybrid analysis

Interaction between full-length UvrB and UvrC proteins was probed using the Bacterial Adenylate Cyclase Two Hybrid (BACTH) system in *E. coli* (48). For this purpose, the *uvrB* and *uvrC* genes were cloned into the pEB354 and pEB355 to be expressed as fusion proteins respectively with the T25 and T18 fragments of adenylate cyclase. The reporter strain BTH101 was co-transformed with the two plasmids, one encoding the T18-bait fusion protein and the other encoding the T25-prey fusion protein (or empty plasmids expressing T18 or T25 alone as controls), and transformants were selected on LB agar plates supplemented with ampicillin and kanamycin incubated at 30°C for 48 h. Five 3 ml LB cultures containing ampicillin, kanamycin and 0.5 mM IPTG, were then inoculated with individual colonies from each transformation plate and incubated in a shaking incubator overnight at 30°C. The next day, 3 μl from each culture were spotted in duplicate on lactose-containing MacConkey (Sigma) agar plates supplemented with ampicillin and kanamycin, which were placed at 30°C for 48 h. Lactose fermenting bacteria, resulting from bait-prey interaction, are red in color. In contrast, the absence of interaction results in beige colonies.

DNA substrates and incision assay

All DNA oligonucleotides were ordered from MWG Biotech and their sequences are provided in Table S3. Incision activity measurements were performed using duplexed 50 mer dsDNA oligonucleotides composed of a 5′-ATTO633-labelled strand containing a fluorescein conjugated thymine in position 26 (strand name: 5′-ATTO633-F26-seq1) annealed with an unlabelled complementary strand (strand name: Rev-seq1). As described previously (45), for the incision assay, 25 nM F26-seq1 dsDNA substrate was incubated at 37°C for 5 min with 1 μM UvrA1, 0.5 μM UvrB and 2 μM UvrC in 50 mM Tris–HCl pH7.5, 50 mM KCl, 5 mM DTT and 2.5 mM $MgCl_2$, before initiating the incision reaction with the addition of 2.5 mM ATP. The reactions were stopped by addition of 10 μl stop buffer to 10 μl reaction mix and subsequent heating of the samples to 95°C for 5 min. To prepare 3′ incised DNA substrate, 25 nM F26-seq1 dsDNA substrate was incubated at 37°C for 1h with 1 μM UvrA1, 0.5 μM UvrB and 2 μM UvrC-Δ(HhH)$_2$ in 50 mM Tris–HCl pH7.5, 50 mM KCl, 5 mM DTT, 2.5 mM $MgCl_2$ and 2.5 mM ATP, before heat inactivation of the proteins at 65°C for 20 min followed by cooling on ice. New reactions were then prepared as described above for the F26-seq1 substrate. All reactions were then analyzed on 20% TBE–8 M urea acrylamide gels pre-run at 5 W/gel in 1× TBE buffer. The gels were run for 35 min and the DNA bands were visualized and quantified on a Chemidoc MP imager (Bio-Rad) using the appropriate excitation light and detection filters for the green and red fluorophores respectively and the ImageLab software (Bio-Rad). All experiments were performed at least three times and the mean values and standard deviation were plotted using GraphPad Prism 8. Statistical analysis of the data was performed in GraphPad Prism 8 using the Dunnett's multiple comparison test. Kinetics data of product (12 or 30 mer fragments) release were fitted to a sigmoidal model in GraphPad Prism 8 ($Y = A/[1 + (1/(k_{obs}*X)^h)]$) in which A is the amount of processed DNA (i.e. $Y_{max} - Y_{min}$), k_{obs} is the observed rate of product release (in min^{-1}), and h is the Hill coefficient. All fits were very good with R^2 values >0.98.

MALDI-ToF mass spectrometry analysis

For MALDI-ToF mass spectrometry analysis, incision reactions containing 2.5 pmol DNA in 100 μl reaction buffer were stopped at 60 min by heating samples to 95°C for 5 min and were desalted using Ziptip column with 0.6 μl C_{18} resin (Millipore). The columns were rinsed with 10 μl water to remove the reaction buffer. The DNA was eluted with 10 μl 50% acetonitrile. 1 μl of matrix solution 3-HPA mixed with 1 μl of oligonucleotide sample were spotted onto a polished stainless MALDI target plate (Bruker) and dried under vacuum. Mass spectra were obtained with a MALDI-ToF Microflex™ spectrometer (Bruker) operated in negative ion mode. Mass spectra of the individual oligonucleotides have been reported earlier (45).

DNA binding assays

Equilibrium fluorescence polarization DNA binding assays were performed on a Clariostar (BMG Labtech) microplate reader, fitted with polarization filters. The DNA substrate consisted of 50 mer dsDNA containing a fluorescein-conjugated thymine in position 26, named 50mer-F26, obtained by annealing For-F26-seq1 with Rev-seq1 (Table S3). 0 to 2 µM UvrB, UvrC full-length and deletion constructs or UvrB/UvrC complex were titrated into 2 nM 50mer-F26 DNA in binding buffer composed of 50 mM Tris–HCl pH 7.5, 50 mM KCl, 5 mM DTT, 0.01% Tween 20, 2.5 mM MgCl$_2$ supplemented with 0.1 mg/ml BSA. When stated, 2.5 mM ATP was also included in the reaction buffer. Reaction volumes were set to 50 µl. In all cases, after subtracting the polarization values obtained for DNA alone, the mean data from at least three independent experiments were fitted to a standard binding equation ($Y = B_{\mathrm{max}} * X^h/(K_{\mathrm{d}}{}^h + X^h)$) assuming a single binding site with Hill slope (h) using GraphPad Prism 8, where Y is the difference between the polarization of completely bound and completely free oligo, X is the protein concentration and K_{d} is the equilibrium dissociation constant. All fits were very good with R^2 values >0.98. Statistical analysis of K_{d} values was performed in GraphPad Prism 8 using an unpaired t-test.

Crystallization, X-ray data collection, structure determination, homology modelling and structure prediction

Crystals of UvrC-C were obtained by vapor diffusion, by mixing and equilibrating UvrC-C protein solution at a concentration of 20 mg/ml with a reservoir solution containing 24–26% PEG 5000 MME or PEG 3350 and 0.1M Bis–Tris pH 6.5. Crystals were cryoprotected in mother liquor supplemented with 20% glycerol and flash-frozen in liquid nitrogen. X-ray diffraction data were collected at 100 K on beamline ID14-EH4 at the European Synchrotron Radiation Facility (ESRF). Diffraction data were integrated using XDS (49) and scaled with SCALA (50). All diffraction data were twinned, so Truncate (50) and Detwin (51) were used to estimate the twin fraction and detwin the data. A complete dataset was collected to 1.80 Å. Phases were calculated by molecular replacement using Phaser (52), using the crystal structures of the C-terminal RNase H and Helix-hairpin-Helix (HhH) domains of *T. maritima* UvrC (TmUvrC) as search models (PDB: 2NRT; (26)). Models of both domains (residues 367–546 and 550–608 respectively) could be built using Coot (53,54) and were refined using Refmac (55). A summary of the data collection parameters and processing and refinement statistics is given in Table 1. Coordinates and structure factors have been deposited in the PDB (PDB: 8B0Q). A homology model of the N-terminal GIY-YIG endonuclease domain of *D. radiodurans* UvrC (UvrC-NEndo) was generated using SWISS-MODEL (56) and *T. maritima* UvrC-NEndo in its Mn-bound state (PDB: 1YD5) as a template. The UvrC-NEndo of *D. radiodurans* and *T. maritima* share 45.5% sequence identity. The sequence of DrUvrC was submitted to AlphaFold2 (57) via the Colaboratory service from Google Research (https://colab.research.google.com/github/sokrypton/ColabFold/blob/main/beta/AlphaFold2_advanced.ipynb). AlphaFold2 generated five very similar, high-confidence models of DrUvrC (Supplementary Figure S1). Structural figures were prepared with Chimera (58) and ChimeraX (59).

Table 1. Crystallographic data collection and refinement statistics of UvrC-C

Data collection & refinement statistics	UvrC-C
Space group	$P2_1$
Unit cell dimensions	$a = 50.4$ Å, $b = 40.8$ Å, $c = 59.6$ Å, $\beta = 90.005°$
Beamline, facility	ID14-4, ESRF
Wavelength (Å)	0.979
Resolution range (Å)	40.81–1.80 (1.90–1.80)
R_{merge} (%)	6.5 (31.0)
Mean (I)/σ(I)	13.7 (4.0)
Completeness (%)	99.6 (98.2)
Twin fraction	0.3
Measured reflections	89 441 (11 622)
Unique reflections	21 462 (3087)
$R_{\mathrm{fact}}/R_{\mathrm{free}}$ (%)	16.6/20.6
Mol/asu	1
Average B factor (Å^2)	25.4
Rms deviations	
Bonds (Å)	0.020
Angles (°)	1.846
Ramachandran (%)	
Favored	98.0
Allowed	2.0
Outliers	–
PDB code	8B0Q

Values in parentheses are for the highest resolution shell.

Resonance Raman spectroscopy

Resonance Raman (RR) spectra were acquired with a Raman spectrometer (LabRam HR), equipped with a 1200 lines/mm grating and a liquid-nitrogen-cooled CCD detector. An Olympus 20× objective was used for laser focusing onto the sample and light collection in the backscattering geometry. Spectra were measured using 406 nm excitation from Kr$^+$ ion laser (Coherent Innova 302). The RR spectra of anaerobically (125 µM) or aerobically (255 µM) purified DrUvrC, were acquired at 77 K using a 2 µl aliquot of the sample placed onto a microscope stage (Linkham THMS 600, Tadworth, UK), which was cooled to 77 K with liquid N$_2$. Experiments were performed using 3 mW laser power and accumulation time of 60 s. Up to four spectra were co-added in each measurement to improve the signal-to-noise ratio (S/N).

Electrochemistry

Cyclic voltammetry (CV) measurements were performed in a conventional three electrode electrochemical cell composed of an Ag/AgCl (3 M, KCl) reference electrode (+0.21 V versus SHE, WPI), a platinum counter electrode (Radiometer) and an Au working electrode (BASi). The supporting electrolyte, 50 mM Tris–HCl pH 7.5 and 100 mM NaCl, was purged with argon before the experiments. The working electrode was subjected to piranha solution for ∼3 min, polished with 1, 0.3 and 0.05 µm alumina slurries, and cleaned in a ultrasounds water bath for ∼5 min. The electrode was then rinsed with water, dried with compressed air and functionalized by immersion for ∼16 h in a 1 mM solution of 11-mercaptoundecanoic acid (MUA) dissolved in ethanol to form a self-assembled monolayer (SAM). For protein attachment to the SAM surface, a droplet of

Table 2. SEC-MALLS derived elution volumes and molecular masses of UvrC constructs

	Major SEC elution peak			2nd minor SEC elution peak		
Protein/[NaCl] (M)/Theo. MW (kDa)	Elution vol. (ml)	MW (kDa)	Oligomeric state (%)	Elution vol. (ml)	MW (kDa)	Oligomeric state (%)
BSA/0.3M/66.0	14.1	54.6	Monomer (79%)	12.2	95.8	Dimer (21%)
BSA/1M/66.0	13.9	57.3	Monomer (71%)	12.0	76.2	Dimer (29%)
UvrC^{WT}/0.3M/69.5	14.0	56.5	Monomer (92%)	11.8	ND*	*Dimer?* (8%)
UvrC^{WT}/1M/69.5	13.4	64.8	Monomer (94%)	11.4	100.0	Dimer (6%)
UvrC-Δ(HhH)$_2$/0.3M/62.1	14.5	56.1	Monomer (99%)	12.4	ND*	*Dimer?* (1%)
UvrC-Δ(HhH)$_2$/1M/62.1	13.9	56.9	Monomer (87%)	11.9	105.0	Dimer (13%)
UvrC-C/0.3M/28.0	16.0	26.0	Monomer (100%)	-	-	-
UvrC-NEndo/0.3M/11.1	18.0	9.8	Monomer (100%)	-	-	-

*Signal too weak for reliable MW determination (<3μg protein in peak)

protein solution (12 mg/ml) was deposited on the electrode surface for ∼20 min; after the protein incubation the electrodes were thoroughly rinsed with buffer to remove non-bound molecules. Electrode potentials were controlled by a Princeton Applied Research 263A potentiostat. Scan rate dependence was performed in the range of 10–2000 mV/s; ET rate constant was determined using Laviron method (60).

RESULTS

Biophysical characterization of *Deinococcus radiodurans* UvrC

UvrC domain organization. D. radiodurans UvrC (DrUvrC) is a 617 amino acid protein composed of a N-terminal GIY-YIG endonuclease domain (NEndo) corresponding to residues 1–80, a central region of unknown function bearing a cysteine (Cys)-rich metal binding site and the UvrB-binding motif, an RNase H endonuclease domain corresponding to residues 367–546, and a C-terminal (HhH)$_2$ motif covering residues 550–608 (Figure 1A and Supplementary Figure S2). To dissect the roles of these respective regions in the dual incision of damaged DNA by the NER system, four deletion constructs of DrUvrC were prepared (Figure 1A) and successfully purified (Supplementary Figure S3) in addition to the full-length UvrC construct: (i) a C-terminally truncated form, missing the (HhH)$_2$ motif and referred to as UvrC-Δ(HhH)$_2$, (ii) the N-terminal half of DrUvrC, named UvrC-N, including the NEndo domain and the central uncharacterized region, (iii) the C-terminal half of DrUvrC, namely UvrC-C, composed of the RNase H domain and the double (HhH)$_2$ motif and finally (iv) the NEndo domain alone, UvrC-NEndo.

Oligomerization state of UvrC. To determine the oligomeric state of DrUvrC, we performed size-exclusion chromatography (SEC) coupled to multi-angle laser light scattering (MALLS) on the various UvrC constructs (Figure 1A). Full-length UvrC and UvrC-Δ(HhH)$_2$ were found to form both monomers and dimers in solution with a majority of protein adopting a monomeric form (Table 2 and Supplementary Figure S4). In the case of UvrC-Δ(HhH)$_2$, the abundance of the dimeric form was increased at higher salt concentrations, suggesting that the monomer-monomer interface likely involves hydrophobic residues (Table 2). In contrast, UvrC-NEndo and UvrC-C constructs were exclusively monomers (Table 2 and Supplementary Figure S4), suggesting that the region responsible for dimerization is located between the GIY-YIG domain and the C-terminal half. UvrC-N interacted non-specifically with the SEC column and could unfortunately not be used for SEC-MALLS analysis.

Metal binding site. Purified UvrC has a distinctive dark brown color at high concentrations, showing an absorption peak around 410 nm, which is characteristic of iron-sulfur (FeS) cluster containing proteins. To further characterize the nature of this FeS cluster, we performed resonance Raman (RR) spectroscopy on aerobically and anaerobically purified DrUvrC. RR spectra are highly sensitive to the cluster type, structure, symmetry and ligand type, allowing for a straightforward identification of the cluster geometry (61–64). The identification of the cluster type is commonly based on the frequency of the most intense vibrational mode (e.g. $A_1{}^b$ mode in [3Fe–4S] and [4Fe–4S] type clusters). For both samples, the RR spectra exhibited an intense band at 346 cm^{-1} (Figure 1B), indicative of $A_1{}^b$ mode of a [3Fe–4S] cluster, and no band around 336 cm^{-1} (or possibly shifted by a few wavenumbers in the case of non-all-cysteinyl coordination) characteristic of $A_1{}^b$ mode of a [4Fe–4S] cluster (61–65). This strongly suggests that DrUvrC houses a [3Fe–4S] cluster, although we cannot fully rule out that an originally formed short lived [4Fe–4S] cluster, carrying a non-cysteinyl fourth ligand, rapidly decays to a more stable [3Fe–4S] state. This is clearly distinct from *E. coli* UvrC (EcUvrC), which has been reported to possess a [4Fe–4S] cluster (33). However, it is in agreement with the finding that DrUvrC bears only three of the four conserved cysteines in the Cys-rich motif located just after the NEndo domain (Supplementary Figure S5), which is the likely binding site for this FeS cluster. The consensus sequence of the Cys-rich motif is $CX_{6\text{-}14}CX_3H/QX_3CX_3C$, where C corresponds to a cysteine and X to any amino acid. The sequence between the second and third cysteines is highly conserved (Supplementary Figure S5). DrUvrC is missing the first cysteine in this motif, which is replaced by an asparagine (N145). Although several residues in the vicinity of N145 could potentially act as the fourth non-cysteinyl ligand, notably S146 and K144 (Supplementary Figure S5), we observe no spectroscopic evidence for this scenario. The binding to the cluster likely involves only the three cysteines (C157, C165 and C169; Supplementary Figure S5). It is noteworthy that the RR spectra of DrUvrC purified in aerobic and anaerobic conditions were very similar, suggesting that the cluster is stable in the presence of oxygen, unlike that of EcUvrC (33). The electrochemical response of DrUvrC's FeS cluster was evaluated by cyclic voltammetry (CV), employing the protein immobilized on gold electrodes modified with MUA-terminated SAMs (Figure 1C). After an initial decay (monitored for ca. 20 scans at 50 mV s^{-1}), the CV signals stabilized, allowing for analysis over a broad scan rate range. The estimated reduction potential, $E_0' = 70 \pm 20$ mV, was found to be constant over the whole tested range and comparable to that of the [4Fe–4S] cluster of EcUvrC (33,62). Note that the values of E_0' of $[4Fe–4S]^{1+/2+}$ and $[3Fe–4S]^{0/1+}$ containing proteins largely overlap (61). The heterogeneous electron transfer rate constant, also derived from the scan-rate-dependent measurements ($3.2 \pm 0.2\ s^{-1}$) is indicative of a slow electron transfer.

UvrC binding to UvrB and DNA

UvrC binding to UvrB. To shed light on the process by which DrUvrC is recruited to the site of DNA damage, we examined its ability to interact with *D. radiodurans* UvrB (DrUvrB). Bacterial two hybrid experiments confirmed that UvrC and UvrB could form a stable complex (Figure 2A). We then used SEC to assess complex formation between UvrB and the various UvrC constructs (Figure 2B–D). When mixed in a 1:1 ratio with UvrB, UvrC formed a stable complex that eluted as a single peak at an elution volume of 12.8 ml, compared to a volume of 13.2 ml for UvrB alone (Figure 2B, C and Supplementary Figure S6). The UvrB/UvrC complex can thus form in solution in the absence of DNA, unlike the *D. radiodurans* UvrA1/UvrB complex that does not stably assemble in similar conditions (Supplementary Figure S6). Likewise the UvrC-$\Delta(HhH)_2$ and UvrC-N constructs also formed complexes with UvrB (Figure 2B, C). The stability of the UvrB/UvrC-$\Delta(HhH)_2$ complex was comparable to that formed by intact UvrC indicating that the $(HhH)_2$ domain is not needed for binding to UvrB (Figure 2C). In contrast, the complex formed between UvrC-N and UvrB was clearly less stable, with only a fraction of the UvrC-N protein co-eluting with UvrB (Figure 2C). The absence of the C-terminal RNase H domain thus destabilizes the UvrB/UvrC complex. Finally, we tested the binding of UvrB to UvrC-C and UvrC-NEndo, but no co-elution was observed (Figure 2D). The UvrC-C and UvrC-NEndo regions eluted as single peaks at respectively 14.9 ml and 16.4 ml (Figure 2B), confirming that the major UvrB-binding region is indeed located between the NEndo domain and the C-terminal RNase H domain. Accordingly, this region comprises the four-helix bundle and in particular the predicted UvrB-binding motif (Figure 1A).

UvrC binding to dsDNA. Next, we compared the DNA binding properties of UvrB, UvrC and UvrB/UvrC using fluorescence polarization. Experiments were performed using a 50 mer dsDNA duplex containing a fluorescein-conjugated thymine in position 26, a substrate known to be efficiently recognized and processed by the UvrABC system (3,45). Alone UvrB is known to bind preferentially to ssDNA (17,19,20,66), and as for other UvrB homologues, DrUvrB also showed relatively weak binding to dsDNA with a Kd of 0.6 μM (Table 3, Figure 2E and Supplementary Figure S7). In contrast, UvrC bound tightly to the 50mer-F26 dsDNA substrate with a K_d of 28 nM in the presence of ATP (Figure 2E), corresponding to the conditions used for the incision reaction, or 40 nM in the absence of ATP (Table 3). In both cases, the binding curves revealed a significant cooperativity in the binding of UvrC to DNA with Hill coefficients close to 2. Next, we examined the binding of the deletion constructs of UvrC to dsDNA. To our surprise, despite lacking the $(HhH)_2$ domain, UvrC-$\Delta(HhH)_2$ bound 50mer-F26 DNA with a K_d of 40 nM, only slightly higher than that of intact UvrC, indicating that the $(HhH)_2$ motif is not the major DNA binding site in UvrC (Table 3, Figure 2E and Supplementary Figure S7). In contrast, UvrC-N and UvrC-C displayed severely impaired DNA binding properties with Kd values of respectively 0.4 and 1.6 μM (Table 3 and Figure 2E), indicating that both regions of UvrC are needed for stable association of UvrC with DNA. This dual binding mode could explain the observed cooperativity of intact UvrC. UvrC-N showed nonetheless significantly stronger binding to dsDNA than the C-terminal half. Finally, we examined the binding of the assembled UvrB/UvrC complex to dsDNA, and found that it displayed the highest affinity for 50mer-F26 DNA with a K_d of 16 nM, which was unaffected by the presence or absence of ATP, although increased cooperativity was detected in the presence of the nucleotide (Table 3, Figure 2E and Supplementary Figure S7).

UvrC dual incision activity

Using the recently established incision assay (Figure 3A) to follow the dual incision activity of the UvrABC system from *D. radiodurans* (45), we probed the activity of the different forms of UvrC. In this assay, the N- and C-terminal endonuclease domains of UvrC perform quasi-simultaneous incision of the substrate DNA respectively on the 3′ and 5′ sides of the damaged nucleotide (in this case, a fluorescein-conjugated thymine) (45). Under these conditions, intermediate products (30 and 32 mer fragments, Figure 3A) are barely detectable and almost 80% of the substrate is processed after 1 h (Figure 3B). In addition to the full-length and deletion constructs of UvrC presented above, we also examined the activity of two point mutants targeting either the conserved glutamate identified as being essential for incision by the NEndo domain (E72), or the first conserved aspartate from the catalytic DDH triad of the C-terminal RNase H endonuclease domain (D391; Supplementary Figure S2) (23,25). In both cases, these residues were mutated to alanine. Interestingly, we observed that both $UvrC^{E72A}$ and $UvrC^{D391A}$ point mutants were unable to cleave the DNA substrate (Figure 3B). Both the 3′ and 5′ cleavage reactions were completely lost in $UvrC^{D391A}$, while in $UvrC^{E72A}$ only a very low residual 5′ cleavage activity could be detected (Figure 3B), suggesting that inactivation of either of the two endonuclease domains in UvrC largely impedes the activity of the remaining active endonuclease domain. The dual

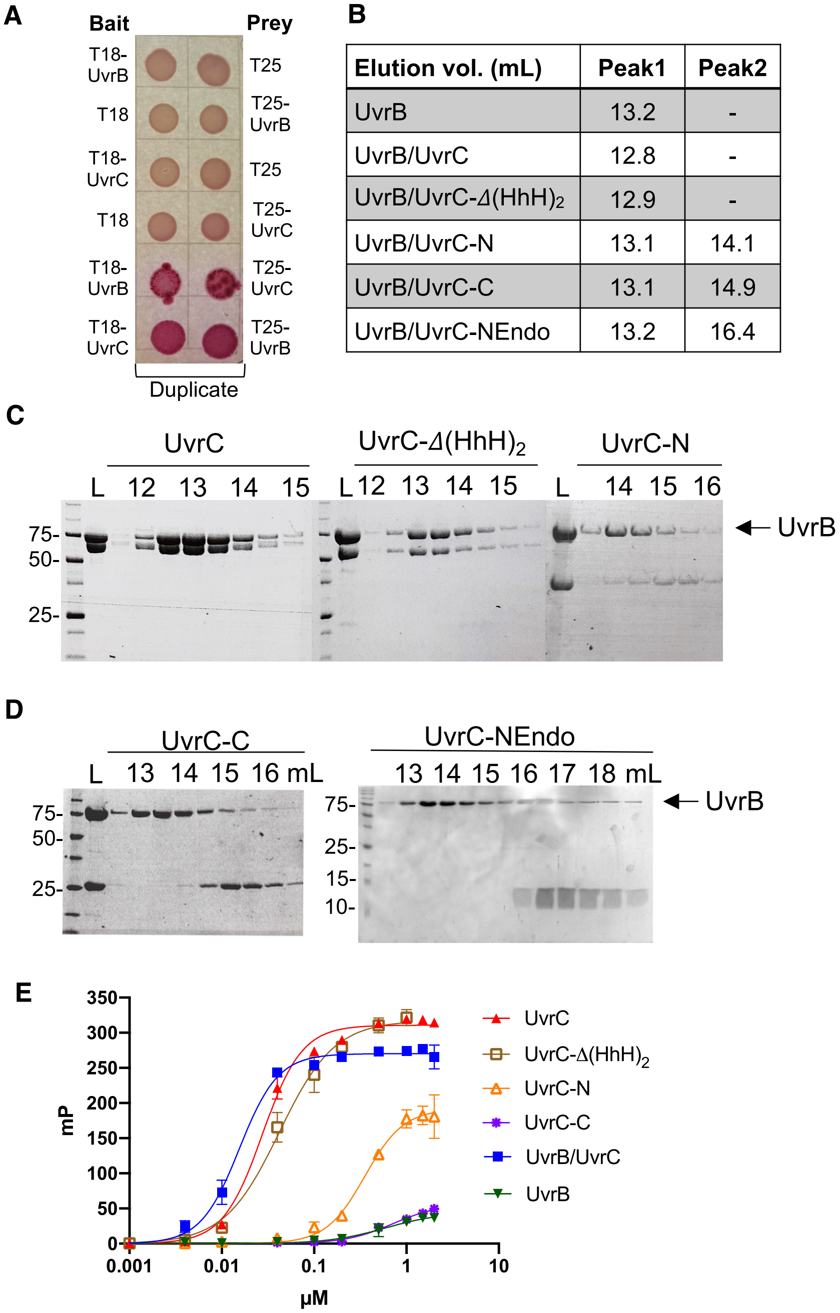

Elution vol. (mL)	Peak1	Peak2
UvrB	13.2	-
UvrB/UvrC	12.8	-
UvrB/UvrC-Δ(HhH)$_2$	12.9	-
UvrB/UvrC-N	13.1	14.1
UvrB/UvrC-C	13.1	14.9
UvrB/UvrC-NEndo	13.2	16.4

Figure 2. Analysis of the interaction between UvrB and UvrC. (**A**) Bacterial two hybrid analysis of the interaction between UvrB and UvrC. For each experiment, a bait and a prey corresponding to UvrB and UvrC proteins fused respectively to the T18 or T25 domains of bacterial adenylate cyclase, or the single T18 and T25 proteins alone, were co-transformed as indicated. Positive interactions were detected on MacConkey agar plates as red colored colonies. The cultures were spotted in duplicate. (**B**) Table presenting the size-exclusion chromatography (SEC) elution volumes of UvrB alone and in complex with different UvrC constructs. (C)-(D) SDS-PAGE analysis of the SEC fractions of the various UvrB/UvrC assemblies listed in (B). (**C**) UvrC constructs containing the N-terminal half of UvrC interact with UvrB. (**D**) UvrC-C and UvrC-NEndo do not interact with UvrB and elute as separate peaks. (**E**) DNA binding curves derived from fluorescence polarization (FP) measurements of 0–2 μM UvrB (green), UvrC (red), UvrC-Δ(HhH)$_2$ (beige), UvrC-N (orange), UvrC-C (purple) or UvrB/UvrC (blue) binding to 2 nM 50 mer dsDNA containing a fluorescein-conjugated thymine in position 26 in the presence of ATP. Data points represent mean and standard deviation of three independent measurements and the data were fitted to a single specific binding model with Hill slope in GraphPad Prism 8. Derived binding constants are presented in Table 3.

Table 3. DNA binding affinity of UvrB, UvrC and UvrB/UvrC complex for 50mer-F26 dsDNA derived from fluorescence polarization measurements

Protein	Nucleotide	K_d (nM) ± SE	Hill coeff.
UvrB	ATP	592 ± 148.0 (*)	1.42
UvrC	ATP	28 ± 1.1	2.02
UvrC	-	40 ± 2.6 (*)	2.18
UvrC-Δ(HhH)$_2$	ATP	42 ± 2.5 (**)	1.46
UvrC-N	ATP	396 ± 22.2 (****)	1.86
UvrC-C	ATP	1610 ± 342.4 (**)	1.46
UvrB/UvrC	ATP	16 ± 0.7 (***)	2.07
UvrB/UvrC	-	18 ± 0.8 (**)	1.47

K_d values that are statistically significantly different from that of UvrC + ATP are indicated with * for a *P* value < 0.05, ** for a *P* value < 0.01, *** for a *P* value < 0.001 and **** for a *P* value < 0.0001. Statistical test: unpaired *t*-test.

endonuclease activities of UvrC thus appear to be tightly coupled. Interestingly, in UvrC^{E72A}, this coupling could be overridden using 3′ incised DNA substrate (Supplementary Figure S8).

To better understand the molecular basis of this coupling, we next compared the activities of wild-type (WT) and catalytically inactive mutants of the isolated domains of UvrC either alone or in combination (Figure 3C and Supplementary Figure S9). The isolated UvrC-NEndo and UvrC-C fragments alone or in combination displayed no incision activity (Figure 3C). In the absence of a UvrB binding domain, these constructs are likely not recruited onto the DNA substrate. In contrast, UvrC-Δ(HhH)$_2$, missing the C-terminal (HhH)$_2$ motif, retained dual incision activity with a wild-type observed rate constant (k_{obs}; Supplementary Table S4) (45). UvrC-Δ(HhH)$_2$ exhibits an intact 3′ incision activity, but a partially impaired 5′ incision activity leading to the progressive accumulation of the 30 mer intermediate fragment resulting from 3′ incision only and a reduced yield of final 12 mer product resulting from the dual incision (Figure 3C and Supplementary Figure S9). This suggests that the (HhH)$_2$ motif is needed for efficient 5′ incision by the C-terminal RNase H domain probably by stabilizing the interaction of UvrC with its DNA substrate, but is entirely dispensable for the 3′ incision. Interestingly, 5′ incision could be fully restored by addition of UvrC-C to the reaction mix containing UvrC-Δ(HhH)$_2$ (Figure 3C, D and Supplementary Figure S9), leading to enhanced dual incision activity (Supplementary Table S4). This intact C-terminal region of DrUvrC could thus compensate for the impaired 5′ incision activity of UvrC-Δ(HhH)$_2$.

More surprisingly, we found that UvrC-N was also able to perform the dual incision reaction with a wild-type-like 3′ incision activity and only a mildly impaired 5′ incision activity, despite the absence of the entire C-terminal RNase H domain responsible for this cleavage reaction (Figure 3C and E and Supplementary Figure S9). A closer look at the kinetics of repair by UvrC-N reveals that its 5′ incision activity is slower than its 3′ incision activity at the start of the kinetics (up to 20 min), leading to the accumulation of small amounts of 30 mer intermediate product, but then the two incisions become synchronized and the final 12 mer yield is comparable to that of intact UvrC (Figure 3E). Since UvrC-N only bears a single endonuclease domain, NEndo, we assume that both incision reactions are catalyzed by the NEndo domain. In agreement with this, we found that the UvrC-N^{E72A} point mutant was completely inactive (Figure 3C). Remarkably, MALDI-ToF mass spectrometry analysis of the reaction products also confirmed that UvrC-N processes the DNA substrate in the same way as UvrC, cleaving the DNA specifically 7 nucleotides upstream and 4 nucleotides downstream of the lesion to release a 12 mer fragment with a phosphate group on the 5′ end, as reported previously (45) (Supplementary Figure S10). Finally, as was observed with UvrC-Δ(HhH)$_2$, wild-type dual incision could be fully restored and even slightly enhanced by addition of UvrC-C to the reaction mix containing UvrC-N (Figure 3C and 3E, Supplementary Figure S9 and Supplementary Table S4).

Finally, to determine whether UvrC-C restores the 5′ incision activity of UvrC-Δ(HhH)$_2$ and UvrC-N through interaction with the N-terminal region of UvrC or instead via binding to the 3′ incised DNA substrate, we evaluated the 5′ incision activity of UvrC-C on a 3′ incised DNA substrate (Supplementary Figure S8). Interestingly, in the presence of UvrA and UvrB, UvrC-C exhibited a robust 5′ incision activity on 3′ incised DNA substrate similar to full-length UvrC, suggesting that UvrC-C is recruited through its binding to the singularly 3′ incised DNA and not through interactions with either UvrC-Δ(HhH)$_2$ or UvrC-N.

UvrC structure

Crystal structure of UvrC-C. UvrC-C, consisting of residues 366–617, was crystallized in space group P2$_1$, containing one monomer per asymmetric unit, and the structure was determined to 1.80 Å resolution by molecular replacement using TmUvrC RNase H and (HhH)$_2$ domains (PDB: 2NRT) as search models (Table 1). The UvrC-C structure comprises the RNase H endonuclease domain, responsible for the 5′ incision event (residues 367–546) and two consecutive HhH motifs forming the (HhH)$_2$ domain (residues 550–608) implicated in DNA binding (Figure 4A). Due to poor electron density, the short linker between the two domains (residues 547–549) could not be built reliably. Similarly, the first (residue 366) and last nine residues (609–617) of this construct are not visible. While the individual domains are structurally homologous to those of TmUvrC-C, with respective root-mean-square deviation (rmsd) values of 1.6 and 1.5 Å and sequence identities of 50 and 36% (Figure 4C), the relative orientation of the RNase H domain with respect to the (HhH)$_2$ domain is very different (Figure 4B). In TmUvrC-C, the (HhH)$_2$ domain is connected to the RNase H endonuclease domain by an α-helix (extension of α4) and a short linker that form a ∼135° kink, which positions the (HhH)$_2$ domain far from the RNase H domain (Figure 4B). In DrUvrC-C, helix α4 is much shorter (Figure 4B-C), and the hinge region (residues 543–552), connecting the two domains, forms an unstructured loop allowing the (HhH)$_2$ domain to fold back onto the RNase H domain partially blocking the access to the active site, although no direct interactions between the two domains are observed (Figure 4B). Despite this different orientation, the active site of the RNase H domain of DrUvrC is very

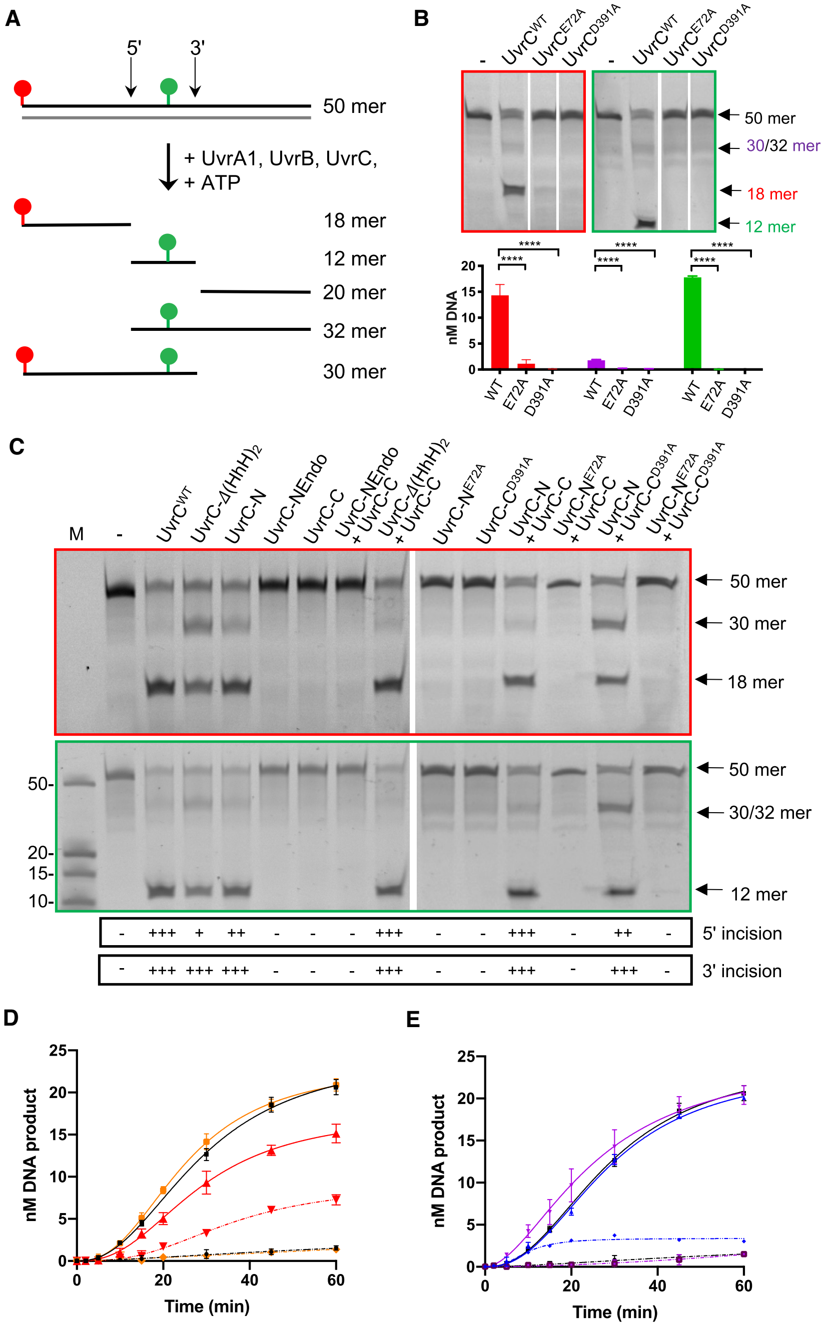

Figure 3. DrUvrABC incision assay. (**A**) Schematic diagram of the DrUvrABC incision assay relying on the use of *D. radiodurans* UvrA1, UvrB and UvrC proteins, ATP and Mg^{2+}, and a dual labelled 50 mer dsDNA substrate containing a red fluorophore (ATTO633) on the 5′ end and a fluorescein conjugated thymine in position 26. (**B**) Representative TBE-polyacrylamide urea gel analysis of the DrUvrABC incision activity of UvrC point mutants. Reactions were performed for 1 hour at 37°C using 25 nM F26-seq1 substrate, 1 μM UvrA1, 0.5 μM UvrB and 2 μM of either $UvrC^{WT}$, $UvrC^{E72A}$ or $UvrC^{D391A}$ in the presence of 2.5 mM Mg^{2+} and 2.5 mM ATP. The major bands observed by electrophoresis using either the red- (left gel) or green- (right gel) filter are indicated with arrows. These experiments were repeated three times and the quantitative assessments of these data are shown below the gels. Histograms present the mean and standard deviation of three independent reactions. Red bars correspond to the 18 mer fragment produced by 5′ cleavage, purple bars to the 30 mer fragment produced by 3′ cleavage, and green bars to the final 12 mer product resulting from dual incision. **** indicates a *P* value < 0.0001. (**C**) Representative TBE-polyacrylamide urea gel analysis of the DrUvrABC incision activity of single or combined UvrC truncation and point mutants. Reactions were performed for 1 hour at 37°C using 25 nM F26-seq1 substrate, 1 μM UvrA1, 0.5 μM UvrB and 2 μM of isolated UvrC domains either alone or in combination in the presence of 2.5 mM Mg^{2+} and 2.5 mM ATP. The major bands observed by electrophoresis using either the red- (top gel) or green- (lower gel) filter are indicated with arrows. These gels were repeated at least three times and the quantitative assessments of these data are presented in Supplementary Figure S9. The extent of 5′ and 3′ incision for each reaction is evaluated as – for no activity, + for low activity, ++ for slightly impaired activity and +++ for WT activity. (**D**) Kinetics of release of 12 mer product (full line) or 30 mer intermediate product (dashed line) by UvrC (black), UvrC-Δ$(HhH)_2$ (red) and UvrC-Δ$(HhH)_2$ + UvrC-C (orange). (**E**) Kinetics of release of 12 mer product (full line) or 30 mer intermediate product (dashed line) by UvrC (black), UvrC-N (blue) and UvrC-N + UvrC-C (purple). (D, E) Data points corresponding to the mean of at least three replicates were fitted to a sigmoidal curve in GraphPad Prism 8.

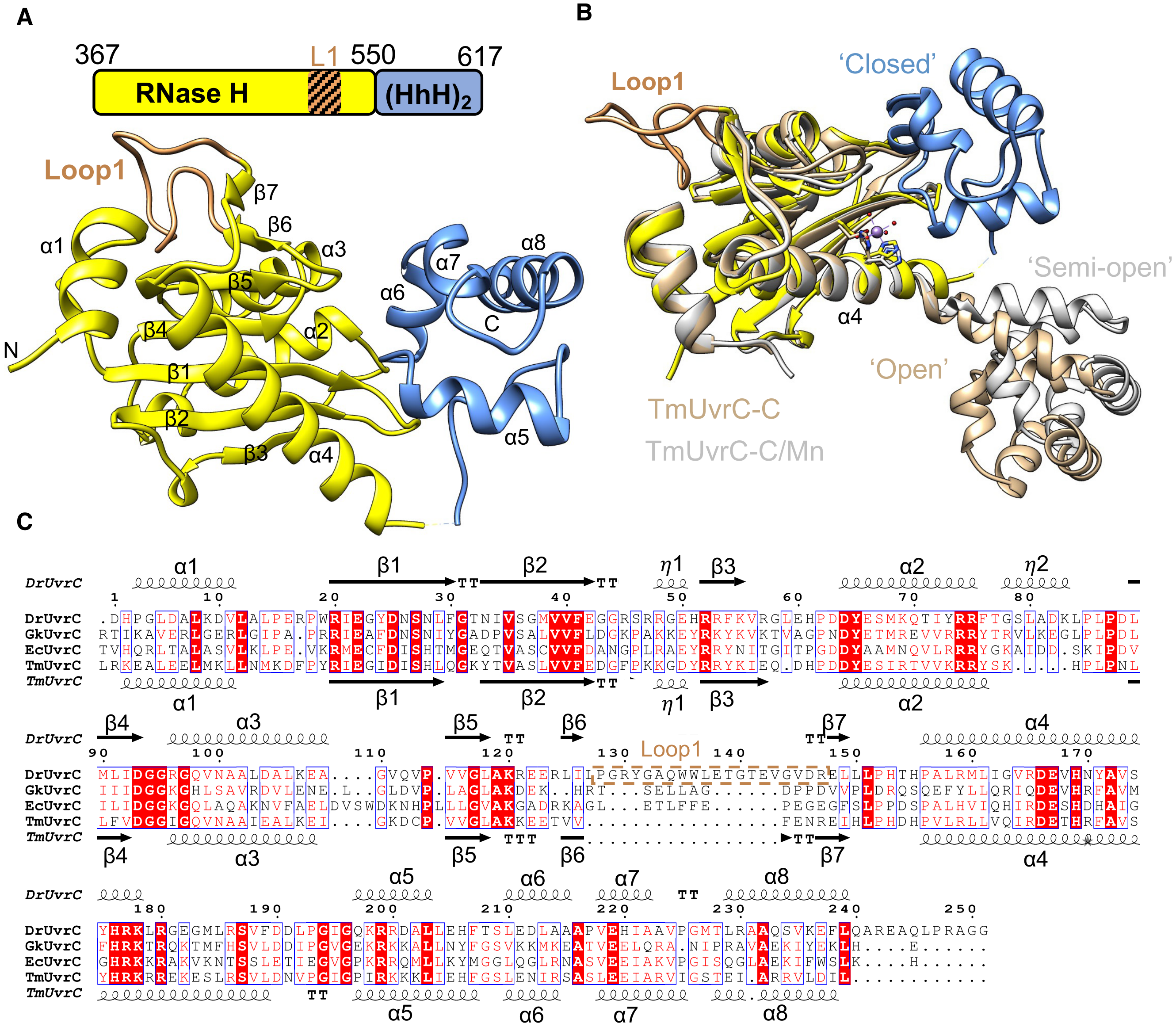

Figure 4. Crystal structure of the C-terminal half of *D. radiodurans* UvrC (UvrC-C). (**A**) Structure of UvrC-C with RNase H domain in yellow and dual $(HhH)_2$ motif in blue. The inserted loop 1 in the RNase H domain is colored in gold. Secondary structure elements are numbered and labelled. (**B**) Overlay of DrUvrC-C with *T. maritima* UvrC-C in either apo- (beige; 'open') or Mn-bound (grey; 'semi-open') states. UvrC-C adopts a more 'closed' conformation in which the flexibly linked $(HhH)_2$ motif folds back onto the RNase H domain blocking access to its active site, illustrated in sticks with the bound Mn ion in purple. (**C**) Sequence alignment of UvrC-C domains from *D. radiodurans*, *G. kaustophilus*, *E. coli* and *T. maritima*.

similar to that of TmUvrC composed of the conserved DDH triad (D391, D459 and H535 in DrUvrC; Figure 4B, C). Although no metal ion was bound in the active site of DrUvrC RNase H domain, the residues are positioned in a very similar conformation as in the Mn-bound structure of TmUvrC (PDB 2NRZ; (26)). This differs from the active site of *G. stearothermophilus* UvrC RNase H domain (PDB: 3C65, unpublished), which is more open due to a shift in the position of the long α4 helix bearing the conserved histidine (Supplementary Figure S11). In the absence of Mn, however, H535 of DrUvrC points away from the two highly conserved aspartate residues (Supplementary Figure S11). A major difference between TmUvrC and DrUvrC is the presence of a 17-residue insertion in between β-strands β6 and β7 of DrUvrC that forms a solvent-exposed loop (Loop1 in Figure 4) pointing away from the active site. This appears to be a particularity of DrUvrC, although short insertions are also observed in this position in other UvrCs (Figure 4C). *Helicobacter pylori* UvrC for example possesses a 13-residue insertion in this position, but the inserted residues are very different from those present in DrUvrC loop1. This loop may thus constitute a site of interaction for species-specific protein partners.

Structural model of full-length UvrC. Two crystal structures of GIY-YIG endonuclease domains of UvrC proteins have previously been reported (25), which display high sequence identity to DrUvrC-NEndo (Supplementary

Figure S2). We therefore built a homology model of this small domain using SWISS-MODEL and TmUvrC-NEndo domain as a template (Supplementary Figure S12). The two models are very similar with a rmsd of 0.3 Å. DrUvrC-NEndo consists of a central three stranded β-sheet surrounded by four α-helices (Supplementary Figure S12). The conserved GIY-YIG motif is strictly conserved between these two models, consisting in both cases of the sequence GVY-YIG (G14, V15, Y16, Y26, I27, G28 in DrUvrC; Supplementary Figure S2). Beyond this motif, the entire active site, and notably the catalytic metal binding glutamate (E72 in DrUvrC, E76 in TmUvrC), is highly conserved with only one difference: Y43 of TmUvrC is replaced by a histidine in DrUvrC (H40), which is found in other UvrC and GIY-YIG family members (25). Manganese or magnesium binding is thus likely to be retained in DrUvrC-NEndo, in agreement with our recent finding that dual incision by DrUvrABC can occur using either magnesium or manganese as a cofactor (45).

Next, we made use of the recently developed structure prediction algorithm, AlphaFold2 (57), to build a high-confidence model of the complete DrUvrC (Figure 5A and Supplementary Figure S1). The high-sequence coverage and large number of available sequences and structures of related domains and proteins in the database allowed AlphaFold2 to produce models of DrUvrC with most regions exhibiting high-confidence scores (Supplementary Figure S1). Regions with confidence scores lower than 70 correspond to either inter-domain regions or to parts of the C-terminal domain. We thus combined our crystal structure of UvrC-C with the predicted structure of UvrC-N to build the first complete model of a UvrC (Figure 5A). The AlphaFold2 predicted model of the UvrC-NEndo endonuclease domain is identical to the homology model we obtained using SWISS-MODEL and TmUvrC-NEndo as a template (Supplementary Figure S12). The predicted model, however, revealed that besides the NEndo domain, UvrC-N was additionally composed of a small β-sheet motif (residues 95–125), a four-helix bundle (residues 126–231), and a second RNase H domain (residues 243–366, named RNase H1, as opposed to the C-terminal RNase H domain hereafter named RNase H2; Figure 5A). Interestingly, in this predicted conformation, access to the active site of the NEndo domain of DrUvrC is also blocked by its tight packing against the RNase H1 domain. In this state, both the N- and C-terminal endonuclease domains of DrUvrC are thus maintained in an inactive state. This may be key to regulate UvrC's function and to avoid unwanted incision activity. DNA incision would necessarily require that UvrC undergoes a major conformational change. The β-sheet motif is connected to the NEndo domain through a 15-amino acid linker, which could certainly provide the necessary flexibility for a major rearrangement of the NEndo domain to allow it to bind its substrate DNA.

The β-sheet motif is a three-stranded anti-parallel β-sheet that is reminiscent of snake venom toxin folds (67) and related mini-protein motifs (68) (Supplementary Figure S13). Beyond acting as a linker domain between the NEndo and the four-helix bundle domains, the function of this motif remains to be identified. The four-helix bundle is composed of helices α5-α8. The conserved Cys-rich motif and its associated FeS cluster are inserted between helices α5 and α6, and protrude away from the core of the enzyme. Beyond a putative role in DNA-mediated charge transfer, the Cys-rich motif and its associated FeS cluster are likely to play a structural role to ensure the correct positioning of the N-terminal domains of UvrC. Helices α7 and α8 of the four-helix bundle correspond to the predicted UvrB-binding motif (69). These helices are structurally very similar to the C-terminal region of UvrB that is responsible for UvrB dimerization through the formation of a four-helix bundle. Several key UvrB dimer interface residues, most of which are hydrophobic, are conserved in UvrC (Figure 5B) and have been shown to contribute to the UvrB/UvrC interface (35). This region may also be responsible for UvrC oligomerization that has been observed under certain conditions (70), as in our SEC-MALLS experiments (Table 2).

Finally, UvrC-N also includes an unexpected RNase H domain, RNase H1, composed of a central five-stranded β-sheet surrounded by three α-helices (Figure 5A and C, and Supplementary Figure S14). This independent domain had not been identified previously by classical bioinformatics tools and yet it is highly conserved and sits at the center of UvrC surrounded by the various other domains. Its fold is very similar to that of the C-terminal RNase H2 domain, despite very low sequence conservation, which may explain why it had not been recognized earlier as an RNase H domain (Figure 5C). Importantly, the three DDH catalytic residues of RNase H2 are not conserved in RNase H1 and are replaced respectively by a glycine, proline and glutamine (Supplementary Figure S14). The RNase H1 domain is thus likely inactive. Similar dual active and inactive RNase H domains are found in viral reverse transcriptase enzymes and some retrotransposons, in which the inactive RNase H domain has evolved to be a tether or connection region (71,72).

Model of UvrC binding to dsDNA. The crystal structure of DrUvrC-C reveals a 'closed' conformation of the C-terminal half of UvrC in which the $(HhH)_2$ domain is closely packed against the RNase H2 domain (Figure 4B). In this conformation, the C-terminal RNase H2 domain is maintained in an inactive state in which DNA binding and cleavage are impossible. By overlaying, on the one hand, the RNase H2 domain of DrUvrC onto *Bacillus halodurans* RNase H domain bound to an RNA/DNA hybrid (PDB: 1ZBI) and, on the other hand, the $(HhH)_2$ domain of DrUvrC onto *E. coli* RuvA bound to dsDNA (PDB: 1C7Y), we were able to build a putative model of UvrC-C bound to duplexed DNA (Figure 6A). To achieve this DNA-bound conformation, the $(HhH)_2$ domain needs to undergo a near 180° anti-clockwise rotation relative to the long α4 helix of the RNase H2 domain (Supplementary Movie S1), which can easily be achieved simply through changes in the conformation of the flexible linker connecting α4 from the RNase H2 domain to α5 in the $(HhH)_2$ domain. This linker also provides sufficient flexibility for the $(HhH)_2$ domain to position itself correctly so as to contact the DNA minor groove notably via its second HhH motif. In this DNA-bound state, the active site of the RNase H2 domain of UvrC-C is correctly positioned relative to the DNA to catalyze the 5′ incision reaction (Figure 6A).

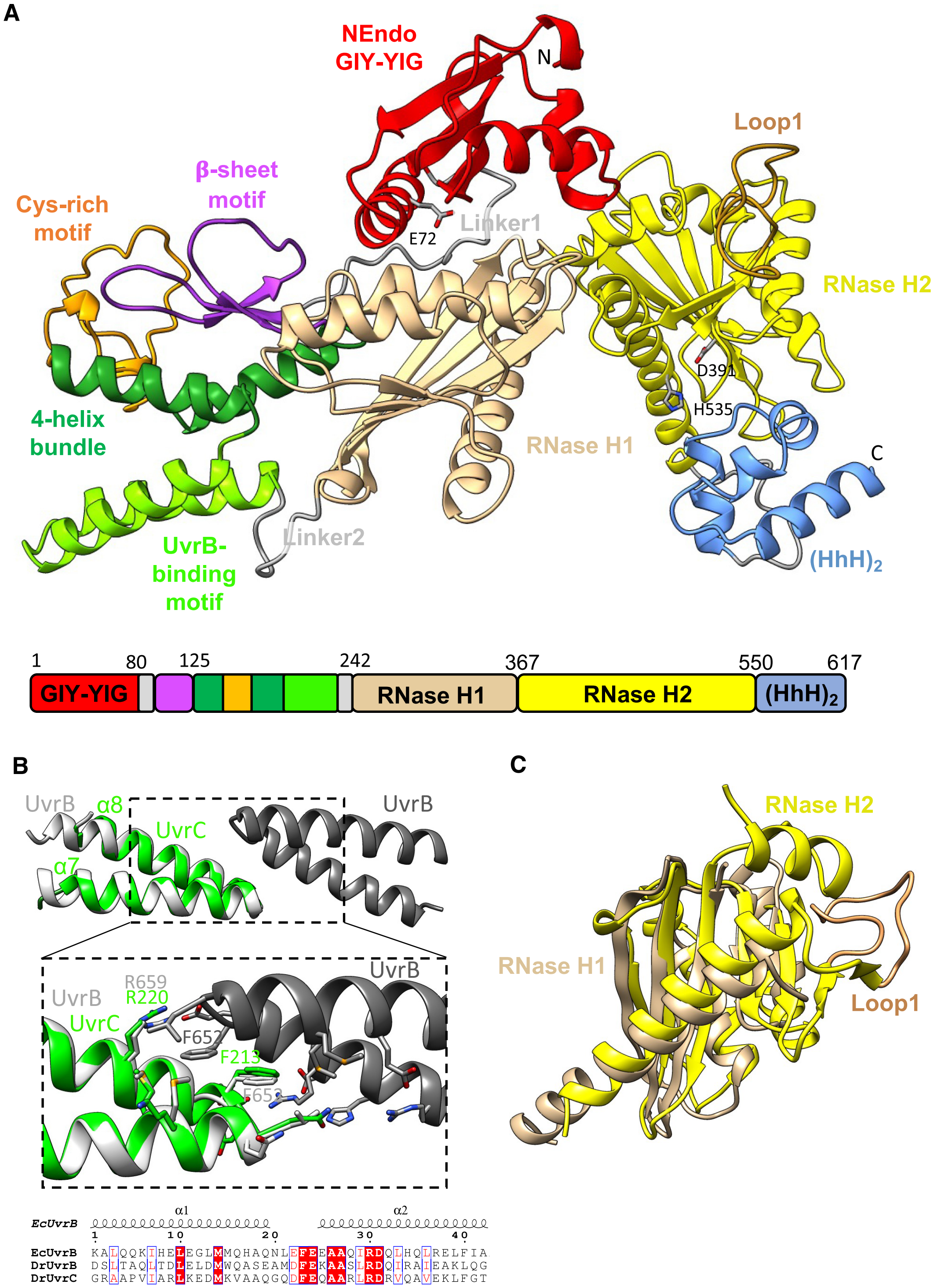

Figure 5. Three-dimensional model of full-length DrUvrC. (**A**) Chimeric model of DrUvrC assembled using the AlphaFold2-predicted model of UvrC-N (NEndo GIY-YIG domain, β-sheet motif, Cys-rich motif, 4-helix bundle and RNase H1 domain) and the crystal structure of UvrC-C (RNase H2 domain and $(HhH)_2$ motif). The different domains are labelled and colored according to the scheme shown below the structure. The central RNase H1 domain (beige) acts as a platform for the other domains and motifs of UvrC. (**B**) Overlay of the predicted UvrB-interacting motif (helices α7 and α8) of DrUvrC (green) with the C-terminal dimerization motif of *E. coli* UvrB (35) (light and dark grey). As shown in the close-up view delineated with a dashed box and in the sequence alignment (presenting sequences of *E. coli* UvrB, *D. radiodurans* UvrB and DrUvrC), several of the interface residues, notably located in the turn between the two helices are conserved. UvrB residues R659 and F652 (equivalent to R220 and F213 in DrUvrC) have previously been shown to play a key role in the UvrB/UvrC interface (35). (**C**) Overlay of the two RNase H domains of DrUvrC. RNase H1 domain is colored beige, while RNase H2 domain is colored yellow. Loop1 of RNase H2 domain is shown in gold.

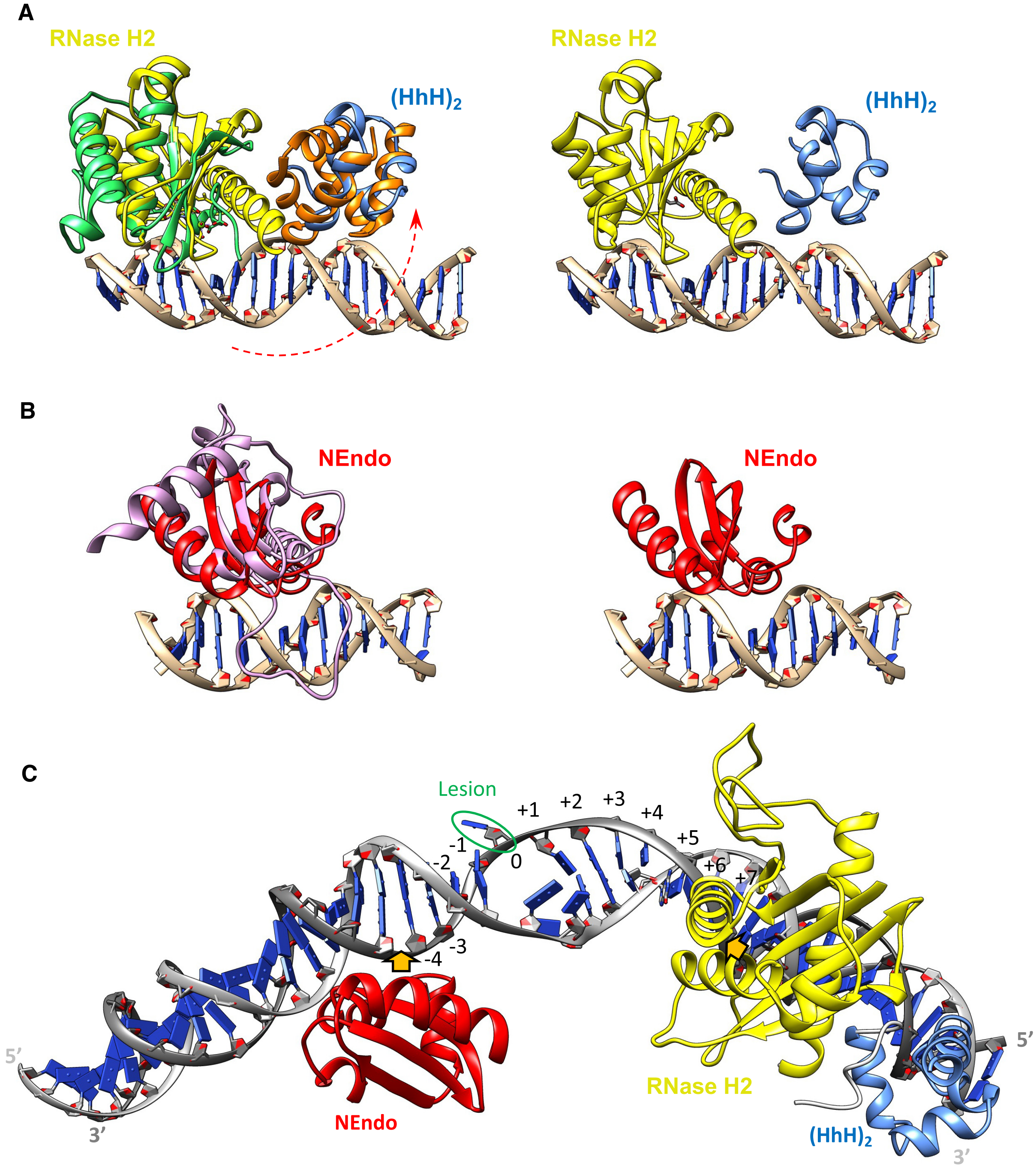

Figure 6. Model of UvrC binding to DNA. (**A**) Model of UvrC-C (yellow and blue) binding to DNA (right) assembled by overlaying (i) the RNase H2 domain of UvrC-C (yellow) onto *Bacillus halodurans* RNase H domain (green) bound to an RNA/DNA hybrid (PDB: 1ZBI) and, (ii) the (HhH)$_2$ domain (blue) of UvrC-C onto *E. coli* RuvA (orange) bound to dsDNA (PDB: 1C7Y) as shown in the left panel. To achieve this DNA-bound conformation, the (HhH)$_2$ motif has to undergo a near 180° anti-clockwise rotation (red dashed arrow) relative to the long α4 helix of the RNase H domain. For clarity, the DNA and RNA/DNA duplexes from the homologous structures are not shown. (**B**) Model of NEndo (red) binding to DNA (right) assembled by overlaying UvrC-NEndo onto *E. coli* GIY-YIG endonuclease R.Eco29kl (purple) bound to DNA (PDB: 3NIC) as shown in the left panel. (**C**) Model of NEndo (red) and UvrC-C (yellow and blue) binding to partially unwound UvrB-bound (not shown for clarity) pre-incision DNA extracted from the co-crystal structure of the *B. caldotenax* UvrB-DNA pre-incision complex (PDB: 6O8F) (73), which we extended on either end with standard B-form duplexed DNA. The flipped out damaged nucleotide is circled in green and the two endonuclease domains are positioned so as to perform their respective incision reactions (indicated with orange arrows) 4 nt downstream (NEndo) and 7 nt upstream (RNase H2) of the damaged site.

Similarly, by overlaying the NEndo domain of DrUvrC onto the structure of *E. coli* GIY-YIG endonuclease R.Eco29kl bound to DNA (PDB: 3NIC), we could build a model of NEndo bound to DNA (Figure 6B). Finally, knowing that the RNase H2 domain incises the DNA 7 nucleotides 5′ to the lesion and that NEndo incises the DNA 4 nucleotides 3′ to the lesion, we could propose a model for the binding of the two endonuclease domains of DrUvrC to duplexed DNA (Figure 6C). To assemble such a model, we used the DNA extracted from the co-crystal structure of the *B. caldotenax* UvrB-DNA pre-incision complex (PDB: 6O8F) (73), which we extended on either end with standard B-form duplexed DNA. This DNA contains an extruded damaged nucleotide and is partially unwound in the vicinity of the lesion. In this proposed model, UvrB and the UvrC endonuclease domains are bound to opposite sides of the DNA duplex and the C-terminal end of UvrB interacts with the helical bundle of UvrC forming a bridge above the DNA duplex (Figures 6C and 7). This model highlights the importance of the intrinsic flexibility of UvrC and to a lesser extent, UvrB, for the formation of this dynamic pre-incision complex.

DISCUSSION

NER is a complex, highly coordinated multi-enzyme repair process that plays a key role in maintaining genome integrity. In the recent years, most studies of bacterial NER have focused on UvrA and UvrB, providing us with a deep understanding of the initial steps of NER (4–6,13,43,74–76). By combining the power of new structure prediction algorithms and experimental crystallographic data, we have assembled the first full model of a UvrC, revealing several unexpected structural motifs and in particular, a central inactive RNase H domain acting as a platform for the surrounding UvrB-, DNA-binding and catalytic domains. Interestingly, in this configuration, access to the active sites of both endonuclease domains is blocked thereby maintaining UvrC in an inactive state (Figure 7), which is likely critical to avoid spurious repair activity that would be highly detrimental to the integrity of the genome. Previously, it had been proposed that UvrB may be responsible for preventing non-specific interaction and incision of the DNA by UvrC (2), but this structure now suggests that in the absence of any partner, UvrC resides in an inactive ‘closed’ state and instead needs to undergo at least two major conformational changes involving both its N- and C-terminal domains to adopt an open conformation that is compatible with binding and incision of its substrate (Figure 7). Such conformational changes would certainly be facilitated by the three flexible hinge regions connecting the NEndo domain to the β-sheet motif, the four-helix bundle to the RNase H1 domain and the RNase H2 domain to the C-terminal $(HhH)_2$ motifs.

The intervention of UvrC in the repair system is initiated following its recruitment to sites of DNA damage by UvrB. Activation of UvrC is thus likely triggered by its binding to UvrB and/or to damaged DNA. UvrB is known to be a central player of NER (17,77). It is involved in damage search along with UvrA (13,77,78), but has also been reported to form a complex with UvrC in solution (79), capable of then binding and hopping along the DNA (34). In the context of NER, it is still unclear whether UvrC is recruited alone to sites of damage or as a complex with UvrB. In *E. coli*, UvrC is not upregulated in response to DNA damage unlike UvrA and UvrB (80), and is thus present at low levels, estimated at 10–20 copies per cell (81,82). UvrB, in contrast, is present in a large excess with ∼2000 copies per cell (80). Under such conditions, given the ability of UvrB and UvrC to interact at low concentrations (34), all the available UvrC in the cell may be bound to UvrB. In this scenario, UvrC is more likely to be recruited as a binary complex with UvrB to sites of DNA damage. In *D. radiodurans,* although the *uvrC* gene is not part of the conserved radiation/desiccation response (RDR) regulon (83,84), its expression has been reported to be upregulated in response to ionizing radiation, but to a lesser extent than the *uvrA*, *uvrB* and *uvrD* genes (85), suggesting that the relative abundance of the UvrABC machinery during the response to DNA damage may be different to that observed in *E. coli* and some UvrC may remain unbound. In this case, UvrC may be recruited directly to UvrB-DNA pre-incision complexes aided by its relatively strong binding affinity for damaged DNA.

In vitro, we found that *D. radiodurans* UvrB and UvrC form a tight complex and our biochemical and structural data fully support the involvement of helices α7 and α8 of the four-helix bundle of UvrC in binding to UvrB, as shown in earlier studies (35,69). We did notice, however, that UvrC-N bearing this UvrB-binding motif exhibited weaker binding to UvrB than full-length UvrC, suggesting that additional regions of UvrC located in the C-terminal region may also contribute to the formation of a stable UvrB/UvrC complex. In the proposed model of UvrC bound to the UvrB-DNA pre-incision complex presented in Figure 7, although the position and orientation of the central RNase H1 domain of UvrC are still highly speculative at this stage, we can see that both the RNase H1 domain and the inserted loop 1 of the RNase H2 domain could potentially provide additional interaction sites for UvrB.

Interestingly, the UvrB/UvrC complex displays distinct DNA binding properties compared to the individual UvrB or UvrC proteins with a much higher affinity for DNA than UvrB alone and a slightly higher affinity than UvrC alone. Binding of UvrB to the helical bundle of UvrC is indeed likely to affect the conformation of the neighboring domains and in particular the linker region between the NEndo domain and the Cys-rich region of UvrC, which in turn may release the NEndo domain responsible for 3′ incision from the central RNase H1 domain (Figure 7). This is in agreement with earlier mutational analyses (36,37) and our UvrC-C incision data on 3′ incised DNA that show that interaction of UvrB with UvrC is indeed needed for the 3′ incision, but not for the 5′ incision.

Opening of the UvrC-C to provide access to the C-terminal endonuclease active site may instead be largely driven by DNA binding and facilitated by the hinge linking the RNase H2 domain to the $(HhH)_2$ motif (Figure 7). Docking of UvrC on the DNA via its C-terminal $(HhH)_2$ motif is required for an efficient 5′ incision activity, but is dispensable for the 3′ incision reaction. Indeed, the 5′ incision activity of UvrC-$\Delta(HhH)_2$ was reduced, likely as a result of its reduced binding affinity for DNA. The $(HhH)_2$

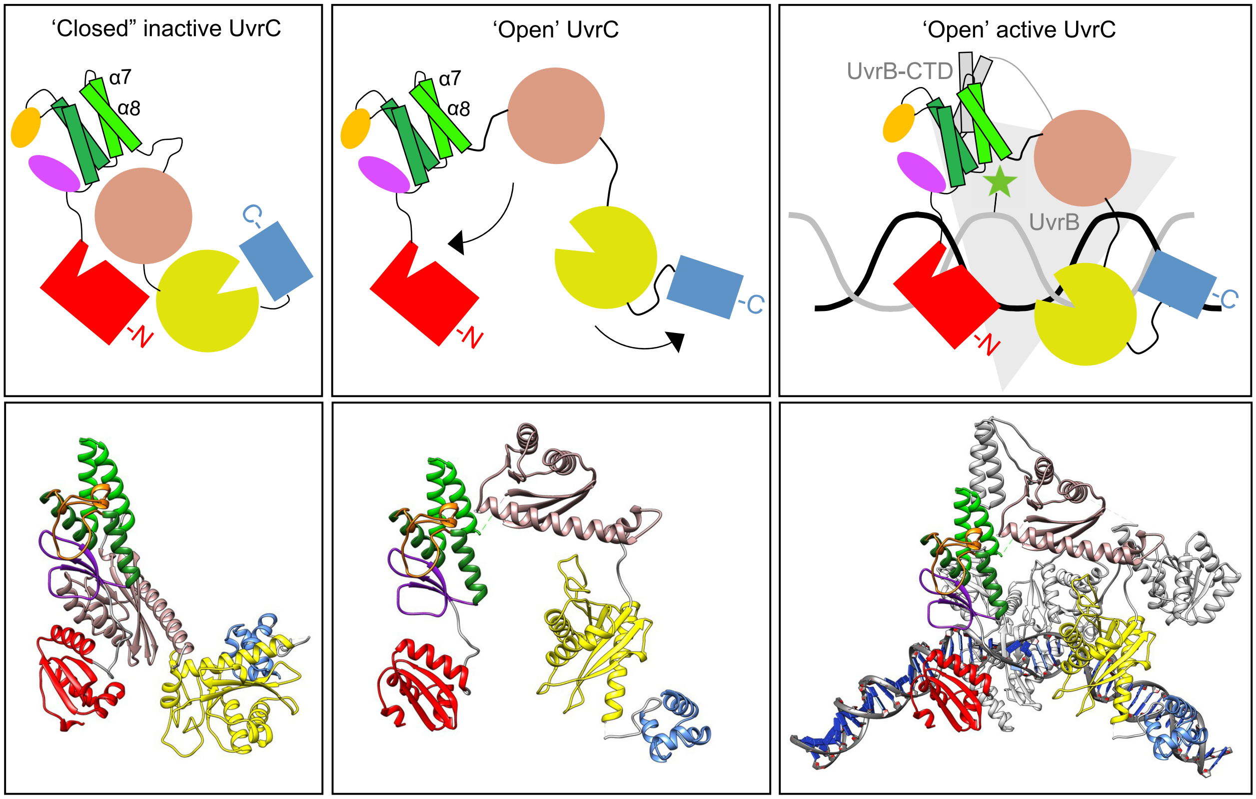

Figure 7. Proposed models of UvrC activation upon UvrB and DNA binding and formation of the UvrB/UvrC pre-incision complex. Alone, UvrC adopts a closed, inactive state (left panel) where access to the active sites of its two endonuclease domains is blocked. Upon binding to UvrB and DNA, UvrC is proposed to undergo a major conformational change, permitted by the flexible linkers between its domains, to adopt a more open and extended conformation in which it can both interact with the C-terminal domain of UvrB (UvrB-CTD) and with the DNA (middle and right panels). Full activation of UvrC additionally requires the partial unwinding of the DNA duplex in the vicinity of the damaged nucleotide by the dual action of UvrA and UvrB. In our present model (right) of the UvrB/UvrC pre-incision complex, although the exact positioning of the central domains of UvrC, and notably the RNase H1 domain, are still only speculative, both the N- and C-terminal regions of UvrC may be in contact with the UvrB-DNA pre-incision complex.

motif is not sufficient in itself to allow tight binding of UvrC-C to DNA, but it may nonetheless stabilize the binding of UvrC, and in particular its C-terminal region, on the DNA substrate after its recruitment to the site of damage. Our fluorescence polarization data revealed that various regions of UvrC contribute to the tight association of UvrC with damaged DNA. Taken individually, each of these regions exhibit relatively low binding affinity for DNA, but when combined in the intact enzyme, they provide tight, cooperative binding to the DNA. It should be noted, however, that in the absence of UvrA (45), as in our DNA binding experiments, although UvrC binds tightly to the DNA, it does not incise the damaged DNA even in the presence of UvrB and ATP, which suggests that binding to UvrB and DNA and formation of an 'open' UvrC are required, but not sufficient to fully activate the endonuclease activities of UvrC. The loading of UvrB onto the DNA by UvrA and the subsequent local unwinding of the DNA duplex around the damaged site by UvrB are also critical to allow the 'open' conformation of UvrC to incise the damaged DNA (Supplementary Figures S8 and S9 and Figure 7).

Beyond the insight provided by our study into the structure and mechanism of action of UvrC endonucleases, this work has also identified several particularities of DrUvrC compared to its previously studied homologues. In *E. coli* and in *T. maritima*, the incision reactions take place in a defined order, first 3′ then 5′ to the lesion, and the two catalytic sites of UvrC can be inactivated independently through site-directed mutagenesis targeting either the NEndo or the RNase H endonuclease catalytic residues leading to impaired 3′ or 5′ incision respectively (24–26,80). In contrast, in the case of *D. radiodurans*, we have previously reported that DrUvrC can perform the dual incision reaction in either order (45) and have found in the present study that the two single point mutants (UvrC^{E72A} and UvrC^{D391A}) were impaired for both 3′ and 5′ incision activities, suggesting that the two active sites are somehow coupled to avoid the formation of unwanted single-strand breaks in the DNA. This coupling can be overridden by using singularly incised DNA as a substrate, indicating that UvrC can sense the DNA conformation and transmit this information between its two distant endonuclease domains. Interestingly, DrUvrC could be separated into two parts (UvrC-N and UvrC-C) which when combined exhibited wild-type UvrC activity, with a highly efficient and quasi-simultaneous dual incision activity, suggesting that the two parts of UvrC do not necessarily need to be covalently linked within a single polypeptide chain to perform their incision reactions. Our data suggests that when separated, UvrC-N is likely recruited to the damaged DNA through its binding to UvrB (and DNA), while UvrC-C relies on its interaction with the 3′ incised DNA.

A second remarkable feature of DrUvrC is the activity of its isolated N-terminal region, UvrC-N. This construct comprising the NEndo domain, the β-sheet motif, the Cys-rich region, the four-helix bundle and the inactive RNase H1 domain, could perform the two incision reactions, albeit with reduced efficiency for the 5′ reaction, cleaving the DNA at the same positions as the intact UvrC enzyme, i.e. 7 nucleotides upstream and 4 nucleotides downstream of the lesion (45). In the absence of a C-terminal endonuclease domain, the two reactions were catalyzed by the NEndo domain. This UvrC-N construct is reminiscent of Cho (UvrC homologue) proteins found in various bacteria (29), but absent in *D. radiodurans*. Cho proteins are homologous to the N-terminal region of UvrC and are classified into five classes according to the different domains that are present (29). Class II Cho proteins, such as *E. coli* Cho, possess a highly conserved GIY-YIG NEndo domain and a Cys-rich motif and can incise DNA on the 3′ side of the lesion, but at the ninth phosphodiester bond instead of the fourth for UvrC (86). Class III Cho proteins additionally possess a UvrB-binding domain and a C-terminal domain, very similar to UvrC-N, and are thus expected to participate directly in NER. Cho proteins have been proposed to broaden the substrate range of NER. *E. coli* Cho, for instance, has been shown to contribute to the repair of interstrand crosslinks (86,87). Although there is no evidence that the N-terminal half of DrUvrC (UvrC-N) functions by itself *in vivo*, these findings hint to an increased plasticity of DrUvrC that could allow it to bind and incise a wider range of helix-distorting lesions. This feature could perhaps explain why DrUvrC, unlike its homologues, can perform the dual incision in either order. Increased catalytic activity and broadened substrate specificity appear to be common traits of *D. radiodurans* DNA repair enzymes (88).

Finally, another particularity of DrUvrC is the nature of its FeS cluster. Unlike EcUvrC that houses an O_2 sensitive [4Fe–4S] cluster, which in aerobic conditions easily degrades into apo species (32), our RR spectra indicate that DrUvrC possesses a [3Fe–4S] cluster that is essentially insensitive to the presence of oxygen. This remarkable difference may confer additional stability to the enzyme under stress conditions.

With this study, we provide important structural and functional insight into the molecular mechanisms underlying UvrC-mediated strand incision during the bacterial NER process. Nonetheless, a number of questions still remain unanswered notably regarding the mode of recruitment of UvrC to the sites of DNA damage, the exact architecture of the UvrB-UvrC-DNA complex, and the roles of the β-sheet, Cys-rich (with its associated FeS cluster) and RNase H1 domains, but also the additional loop1 found in RNase H2 domain, in regulating the activity of UvrC. Further studies will be needed to address these key questions.

DATA AVAILABILITY

Atomic coordinates and structure factors for the reported crystal structures have been deposited with the Protein Data Bank under accession number 8B0Q.

SUPPLEMENTARY DATA

Supplementary Data are available at NAR Online.

ACKNOWLEDGEMENTS

IBS acknowledges integration into the Interdisciplinary Research Institute of Grenoble (IRIG, CEA). This work used the platforms of the Grenoble Instruct-ERIC center (ISBG; UAR 3518 CNRS-CEA-UGA-EMBL) within the Grenoble Partnership for Structural Biology (PSB), supported by FRISBI (ANR-10-INBS-0005–02) and GRAL, financed within the University Grenoble Alpes graduate school (Ecoles Universitaires de Recherche) CBH-EUR-GS (ANR-17-EURE-0003). We acknowledge the European Synchrotron Radiation Facility for provision of synchrotron radiation facilities and we would like to thank the ESRF staff for assistance and support in using beamline ID14-EH4.

FUNDING

Initiative d'Excellence (Idex) University Grenoble Alpes, as part of the Initiatives de Recherches Stratégiques 2017 call [CBS-IRS-2017-TIMMINS-RAVANAT]; Commissariat à l'énergie atomique et aux énergies renouvelables (CEA) [Radiobiology grant]; FCT - Fundação para a Ciência e a Tecnologia, I.P., through MOSTMICRO-ITQB R&D Unit [UIDB/04612/2020, UIDP/04612/2020]; LS4FUTURE Associated Laboratory [LA/P/0087/2020]. Funding for open access charge: Commissariat à l'énergie atomique et aux énergies renouvelables (CEA) and EDF (GGP Sciences du Vivant grant).

Conflict of interest statement. None declared.

REFERENCES

1. Kisker,C., Kuper,J. and Van Houten,B. (2013) Prokaryotic nucleotide excision repair. *Cold Spring Harb. Perspect. Biol.*, **5**, a012591.
2. Kad,N.M. and Van Houten,B. (2012) Dynamics of lesion processing by bacterial nucleotide excision repair proteins. *Prog. Mol. Biol. Transl. Sci.*, **110**, 1–24.
3. Truglio,J.J., Croteau,D.L., Van Houten,B. and Kisker,C. (2006) Prokaryotic nucleotide excision repair: the UvrABC system. *Chem. Rev.*, **106**, 233–252.
4. Jaciuk,M., Swuec,P., Gaur,V., Kasprzak,J.M., Renault,L., Dobrychłop,M., Nirwal,S., Bujnicki,J.M., Costa,A. and Nowotny,M. (2020) A combined structural and biochemical approach reveals translocation and stalling of UvrB on the DNA lesion as a mechanism of damage verification in bacterial nucleotide excision repair. *DNA Repair (Amst.)*, **85**, 102746.
5. Pakotiprapha,D. and Jeruzalmi,D. (2013) Small-angle X-ray scattering reveals architecture and A(2)B(2) stoichiometry of the UvrA-UvrB DNA damage sensor. *Proteins*, **81**, 132–139.
6. Pakotiprapha,D., Samuels,M., Shen,K., Hu,J.H. and Jeruzalmi,D. (2012) Structure and mechanism of the UvrA-UvrB DNA damage sensor. *Nat. Struct. Mol. Biol.*, **19**, 291–298.
7. Mazur,S.J. and Grossman,L. (1991) Dimerization of *Escherichia coli* UvrA and its binding to undamaged and ultraviolet light damaged DNA. *Biochemistry*, **30**, 4432–4443.
8. Thiagalingam,S. and Grossman,L. (1991) Both ATPase sites of *Escherichia coli* UvrA have functional roles in nucleotide excision repair. *J. Biol. Chem.*, **266**, 11395–11403.
9. Timmins,J., Gordon,E., Caria,S., Leonard,G., Acajjaoui,S., Kuo,M.S., Monchois,V. and McSweeney,S. (2009) Structural and mutational analyses of *Deinococcus radiodurans* UvrA2 provide insight into DNA binding and damage recognition by UvrAs. *Structure*, **17**, 547–558.

10. Pakotiprapha,D., Inuzuka,Y., Bowman,B.R., Moolenaar,G.F., Goosen,N., Jeruzalmi,D. and Verdine,G.L. (2008) Crystal structure of *Bacillus stearothermophilus* UvrA provides insight into ATP-modulated dimerization, UvrB interaction, and DNA binding. *Mol. Cell*, **29**, 122–133.
11. Rossi,F., Khanduja,J.S., Bortoluzzi,A., Houghton,J., Sander,P., Guthlein,C., Davis,E.O., Springer,B., Bottger,E.C., Relini,A. *et al.* (2011) The biological and structural characterization of *Mycobacterium tuberculosis* UvrA provides novel insights into its mechanism of action. *Nucleic Acids Res.*, **39**, 7316–7328.
12. Nowotny,M., Jaciuk,M., Nowak,E., Skowronek,K. and Tanska,A. (2011) Structure of UvrA nucleotide excision repair protein in complex with modified DNA. *Nat. Struct. Mol. Biol.*, **18**, 191–197.
13. Stracy,M., Jaciuk,M., Uphoff,S., Kapanidis,A.N., Nowotny,M., Sherratt,D.J. and Zawadzki,P. (2016) Single-molecule imaging of UvrA and UvrB recruitment to DNA lesions in living *Escherichia coli*. *Nat. Commun.*, **7**, 12568.
14. Orren,D.K. and Sancar,A. (1989) The (A)BC excinuclease of *Escherichia coli* has only the UvrB and UvrC subunits in the incision complex. *Proc. Natl. Acad. Sci. U.S.A.*, **86**, 5237–5241.
15. Kad,N.M., Wang,H., Kennedy,G.G., Warshaw,D.M. and Van Houten,B. (2010) Collaborative dynamic DNA scanning by nucleotide excision repair proteins investigated by single- molecule imaging of quantum-dot-labeled proteins. *Mol. Cell*, **37**, 702–713.
16. Theis,K., Chen,P.J., Skorvaga,M., Van Houten,B. and Kisker,C. (1999) Crystal structure of UvrB, a DNA helicase adapted for nucleotide excision repair. *EMBO J.*, **18**, 6899–6907.
17. Truglio,J.J., Karakas,E., Rhau,B., Wang,H., DellaVecchia,M.J., Van Houten,B. and Kisker,C. (2006) Structural basis for DNA recognition and processing by UvrB. *Nat. Struct. Mol. Biol.*, **13**, 360–364.
18. Eryilmaz,J., Ceschini,S., Ryan,J., Geddes,S., Waters,T.R. and Barrett,T.E. (2006) Structural insights into the cryptic DNA-dependent ATPase activity of UvrB. *J. Mol. Biol.*, **357**, 62–72.
19. Waters,T.R., Eryilmaz,J., Geddes,S. and Barrett,T.E. (2006) Damage detection by the UvrABC pathway: crystal structure of UvrB bound to fluorescein-adducted DNA. *FEBS Lett.*, **580**, 6423–6427.
20. Webster,M.P., Jukes,R., Zamfir,V.S., Kay,C.W., Bagneris,C. and Barrett,T. (2012) Crystal structure of the UvrB dimer: insights into the nature and functioning of the UvrAB damage engagement and UvrB-DNA complexes. *Nucleic Acids Res.*, **40**, 8743–8758.
21. Lahiri,S., Rizzi,M., Rossi,F. and Miggiano,R. (2018) *Mycobacterium tuberculosis* UvrB forms dimers in solution and interacts with UvrA in the absence of ligands. *Proteins Struct. Funct. Bioinf.*, **86**, 98–109.
22. Malta,E., Moolenaar,G.F. and Goosen,N. (2007) Dynamics of the UvrABC nucleotide excision repair proteins analyzed by fluorescence resonance energy transfer. *Biochemistry*, **46**, 9080–9088.
23. Lin,J.J., Phillips,A.M., Hearst,J.E. and Sancar,A. (1992) Active site of (A)BC excinuclease. II. Binding, bending, and catalysis mutants of UvrB reveal a direct role in 3' and an indirect role in 5' incision. *J. Biol. Chem.*, **267**, 17693–17700.
24. Verhoeven,E.E., van Kesteren,M., Moolenaar,G.F., Visse,R. and Goosen,N. (2000) Catalytic sites for 3' and 5' incision of *Escherichia coli* nucleotide excision repair are both located in UvrC. *J. Biol. Chem.*, **275**, 5120–5123.
25. Truglio,J.J., Rhau,B., Croteau,D.L., Wang,L., Skorvaga,M., Karakas,E., DellaVecchia,M.J., Wang,H., Van Houten,B. and Kisker,C. (2005) Structural insights into the first incision reaction during nucleotide excision repair. *EMBO J.*, **24**, 885–894.
26. Karakas,E., Truglio,J.J., Croteau,D., Rhau,B., Wang,L., Van Houten,B. and Kisker,C. (2007) Structure of the C-terminal half of UvrC reveals an RNase H endonuclease domain with an Argonaute-like catalytic triad. *EMBO J.*, **26**, 613–622.
27. Thakur,M., Agarwal,A. and Muniyappa,K. (2021) The intrinsic ATPase activity of *Mycobacterium tuberculosis* UvrC is crucial for its damage-specific DNA incision function. *FEBS J.*, **288**, 1179–1200.
28. Verhoeven,E.E., van Kesteren,M., Turner,J.J., van der Marel,G.A., van Boom,J.H., Moolenaar,G.F. and Goosen,N. (2002) The C-terminal region of *Escherichia coli* UvrC contributes to the flexibility of the UvrABC nucleotide excision repair system. *Nucleic Acids Res.*, **30**, 2492–2500.
29. Goosen,N. and Moolenaar,G.F. (2008) Repair of UV damage in bacteria. *DNA Repair (Amst.)*, **7**, 353–379.
30. Shao,X. and Grishin,N.V. (2000) Common fold in helix-hairpin-helix proteins. *Nucleic Acids Res.*, **28**, 2643–2650.
31. Singh,S., Folkers,G.E., Bonvin,A.M.J.J., Boelens,R., Wechselberger,R., Niztayev,A. and Kaptein,R. (2002) Solution structure and DNA-binding properties of the C-terminal domain of UvrC from *E. coli*. *EMBO J.*, **21**, 6257–6266.
32. Tripsianes,K., Folkers,G., Ab,E., Das,D., Odijk,H., Jaspers,N.G.J., Hoeijmakers,J.H.J., Kaptein,R. and Boelens,R. (2005) The structure of the human ERCC1/XPF interaction domains reveals a complementary role for the two proteins in nucleotide excision repair. *Structure*, **13**, 1849–1858.
33. Silva,R.M.B., Grodick,M.A. and Barton,J.K. (2020) UvrC coordinates an O(2)-Sensitive [4Fe4S] Cofactor. *J. Am. Chem. Soc.*, **142**, 10964–10977.
34. Hughes,C.D., Wang,H., Ghodke,H., Simons,M., Towheed,A., Peng,Y., Van Houten,B. and Kad,N.M. (2013) Real-time single-molecule imaging reveals a direct interaction between UvrC and UvrB on DNA tightropes. *Nucleic Acids Res.*, **41**, 4901–4912.
35. Sohi,M., Alexandrovich,A., Moolenaar,G., Visse,R., Goosen,N., Vernede,X., Fontecilla-Camps,J.C., Champness,J. and Sanderson,M.R. (2000) Crystal structure of *Escherichia coli* UvrB C-terminal domain, and a model for UvrB-UvrC interaction. *FEBS Lett.*, **465**, 161–164.
36. Moolenaar,G.F., Franken,K.L., van de Putte,P. and Goosen,N. (1997) Function of the homologous regions of the *Escherichia coli* DNA excision repair proteins UvrB and UvrC in stabilization of the UvrBC-DNA complex and in 3'-incision. *Mutat. Res.*, **385**, 195–203.
37. Moolenaar,G.F., Franken,K.L., Dijkstra,D.M., Thomas-Oates,J.E., Visse,R., van de Putte,P. and Goosen,N. (1995) The C-terminal region of the UvrB protein of *Escherichia coli* contains an important determinant for UvrC binding to the preincision complex but not the catalytic site for 3'-incision. *J. Biol. Chem.*, **270**, 30508–30515.
38. Moolenaar,G.F., Bazuine,M., van Knippenberg,I.C., Visse,R. and Goosen,N. (1998) Characterization of the *Escherichia coli* damage-independent UvrBC endonuclease activity. *J. Biol. Chem.*, **273**, 34896–34903.
39. Sancar,A. and Rupp,W.D. (1983) A novel repair enzyme: UVRABC excision nuclease of *Escherichia coli* cuts a DNA strand on both sides of the damaged region. *Cell*, **33**, 249–260.
40. Visse,R., de Ruijter,M., Brouwer,J., Brandsma,J.A. and van de Putte,P. (1991) Uvr excision repair protein complex of *Escherichia coli* binds to the convex side of a cisplatin-induced kink in the DNA. *J. Biol. Chem.*, **266**, 7609–7617.
41. Visse,R., de Ruijter,M., Moolenaar,G.F. and van de Putte,P. (1992) Analysis of UvrABC endonuclease reaction intermediates on cisplatin-damaged DNA using mobility shift gel electrophoresis. *J. Biol. Chem.*, **267**, 6736–6742.
42. Croteau,D.L., DellaVecchia,M.J., Wang,H., Bienstock,R.J., Melton,M.A. and Van Houten,B. (2006) The C-terminal zinc finger of UvrA does not bind DNA directly but regulates damage-specific DNA binding. *J. Biol. Chem.*, **281**, 26370–26381.
43. Jaciuk,M., Nowak,E., Skowronek,K., Tanska,A. and Nowotny,M. (2011) Structure of UvrA nucleotide excision repair protein in complex with modified DNA. *Nat. Struct. Mol. Biol.*, **18**, 191–197.
44. Mazloum,N., Stegman,M.A., Croteau,D.L., Van Houten,B., Kwon,N.S., Ling,Y., Dickinson,C., Venugopal,A., Towheed,M.A. and Nathan,C. (2011) Identification of a chemical that inhibits the mycobacterial UvrABC complex in nucleotide excision repair. *Biochemistry*, **50**, 1329–1335.
45. Seck,A., De Bonis,S., Saint-Pierre,C., Gasparutto,D., Ravanat,J.-L. and Timmins,J. (2022) *In vitro* reconstitution of an efficient nucleotide excision repair system using mesophilic enzymes from *Deinococcus radiodurans*. *Commun. Biol.*, **5**, 127.
46. Makarova,K.S., Aravind,L., Wolf,Y.I., Tatusov,R.L., Minton,K.W., Koonin,E.V. and Daly,M.J. (2001) Genome of the extremely radiation-resistant bacterium *Deinococcus radiodurans* viewed from the perspective of comparative genomics. *Microbiol. Mol. Biol. Rev.*, **65**, 44–79.
47. Stelter,M., Acajjaoui,S., McSweeney,S. and Timmins,J. (2013) Structural and mechanistic insight into DNA unwinding by *Deinococcus radiodurans* UvrD. *PLoS One*, **8**, e77364.
48. Battesti,A. and Bouveret,E. (2012) The bacterial two-hybrid system based on adenylate cyclase reconstitution in *Escherichia coli*. *Methods*, **58**, 325–334.
49. Kabsch,W. (2010) Xds. *Acta. Crystallogr. D Biol. Crystallogr.*, **66**, 125–132.

50. Winn,M.D., Ballard,C.C., Cowtan,K.D., Dodson,E.J., Emsley,P., Evans,P.R., Keegan,R.M., Krissinel,E.B., Leslie,A.G., McCoy,A. *et al.* (2011) Overview of the CCP4 suite and current developments. *Acta. Crystallogr. D Biol. Crystallogr.*, **67**, 235–242.
51. Yeates,T.O. (1997) Detecting and overcoming crystal twinning. *Methods Enzymol.*, **276**, 344–358.
52. McCoy,A.J., Grosse-Kunstleve,R.W., Adams,P.D., Winn,M.D., Storoni,L.C. and Read,R.J. (2007) Phaser crystallographic software. *J. Appl. Crystallogr.*, **40**, 658–674.
53. Emsley,P. and Cowtan,K. (2004) Coot: model-building tools for molecular graphics. *Acta. Crystallogr. D Biol. Crystallogr.*, **60**, 2126–2132.
54. Emsley,P., Lohkamp,B., Scott,W.G. and Cowtan,K. (2010) Features and development of Coot. *Acta Crystallogr. D*, **66**, 486–501.
55. Murshudov,G.N., Skubak,P., Lebedev,A.A., Pannu,N.S., Steiner,R.A., Nicholls,R.A., Winn,M.D., Long,F. and Vagin,A.A. (2011) REFMAC5 for the refinement of macromolecular crystal structures. *Acta. Crystallogr. D Biol. Crystallogr.*, **67**, 355–367.
56. Waterhouse,A., Bertoni,M., Bienert,S., Studer,G., Tauriello,G., Gumienny,R., Heer,F.T., de Beer,T.A.P., Rempfer,C., Bordoli,L. *et al.* (2018) SWISS-MODEL: homology modelling of protein structures and complexes. *Nucleic Acids Res.*, **46**, W296–W303.
57. Jumper,J., Evans,R., Pritzel,A., Green,T., Figurnov,M., Ronneberger,O., Tunyasuvunakool,K., Bates,R., Žídek,A., Potapenko,A. *et al.* (2021) Highly accurate protein structure prediction with AlphaFold. *Nature*, **596**, 583–589.
58. Pettersen,E.F., Goddard,T.D., Huang,C.C., Couch,G.S., Greenblatt,D.M., Meng,E.C. and Ferrin,T.E. (2004) UCSF Chimera–a visualization system for exploratory research and analysis. *J. Comput. Chem.*, **25**, 1605–1612.
59. Pettersen,E.F., Goddard,T.D., Huang,C.C., Meng,E.C., Couch,G.S., Croll,T.I., Morris,J.H. and Ferrin,T.E. (2021) UCSF ChimeraX: structure visualization for researchers, educators, and developers. *Protein Sci.*, **30**, 70–82.
60. Laviron,E. (1979) General expression of the linear potential sweep voltammogram in the case of diffusionless electrochemical systems. *J. Electroanal. Chem. Interfacial Electrochem.*, **101**, 19–28.
61. Caserta,G., Zuccarello,L., Barbosa,C., Silveira,C.M., Moe,E., Katz,S., Hildebrandt,P., Zebger,I. and Todorovic,S. (2022) Unusual structures and unknown roles of FeS clusters in metalloenzymes seen from a resonance Raman spectroscopic perspective. *Coord. Chem. Rev.*, **452**, 214287.
62. Todorovic,S. and Teixeira,M. (2018) Resonance Raman spectroscopy of Fe-S proteins and their redox properties. *J. Biol. Inorg. Chem.*, **23**, 647–661.
63. Spiro,T.G. and Czernuszewicz,R.S. (1995) Resonance Raman spectroscopy of metalloproteins. *Meth. Enzymol.*, **246**, 416–460.
64. Papadopoulos,P. (2008) Friedrich Siebert and Peter Hildebrandt, vibrational spectroscopy in life science. *Colloid. Polym. Sci.*, **286**, 487–487.
65. Todorovic,S., Leal,S.S., Salgueiro,C.A., Zebger,I., Hildebrandt,P., Murgida,D.H. and Gomes,C.M. (2007) A spectroscopic study of the temperature induced modifications on ferredoxin folding and iron−sulfur moieties. *Biochemistry*, **46**, 10733–10738.
66. Thakur,M., Kumar,M.B.J. and Muniyappa,K. (2016) *Mycobacterium tuberculosis* UvrB is a robust DNA-stimulated ATPase that also possesses structure-specific ATP-dependent DNA helicase activity. *Biochemistry*, **55**, 5865–5883.
67. Hatanaka,H., Oka,M., Kohda,D., Tate,S., Suda,A., Tamiya,N. and Inagaki,F. (1994) Tertiary structure of erabutoxin b in aqueous solution as elucidated by two-dimensional nuclear magnetic resonance. *J. Mol. Biol.*, **240**, 155–166.
68. Ottesen,J. and Imperiali,B. (2001) Design of a discretely folded mini-protein motif with predominantly beta-structure. *Nat. Struct. Biol.*, **8**, 535–539.
69. Moolenaar,G.F., Franken,K.L., Dijkstra,D.M., Thomas-Oates,J.E., Visse,R., van de Putte,P. and Goosen,N. (1995) The C-terminal region of the UvrB protein of *Escherichia coli* contains an important determinant for UvrC binding to the preincision complex but not the catalytic site for 3'-incision. *J. Biol. Chem.*, **270**, 30508–30515.
70. Ms,T., Nazimiec,M., Ye,X., Iyer,G.H., Eveleigh,J., Zheng,Y., Zhou,W. and Tang,Y.Y. (2001) Two forms of UvrC protein with different double-stranded DNA binding affinities. *J. Biol. Chem.*, **276**, 3904–3910.
71. Ustyantsev,K., Novikova,O., Blinov,A. and Smyshlyaev,G. (2015) Convergent evolution of ribonuclease H in LTR retrotransposons and retroviruses. *Mol. Biol. Evol.*, **32**, 1197–1207.
72. Moelling,K., Broecker,F., Russo,G. and Sunagawa,S. (2017) RNase H as gene modifier, driver of evolution and antiviral defense. *Front. Microbiol.*, **8**, 1745 .
73. Lee,S.-J., Sung,R.-J. and Verdine,G.L. (2019) Mechanism of DNA lesion homing and recognition by the Uvr nucleotide excision repair system. *Research*, **2019**, 5641746.
74. Barnett,J.T. and Kad,N.M. (2019) Understanding the coupling between DNA damage detection and UvrA's ATPase using bulk and single molecule kinetics. *FASEB J.*, **33**, 763–769.
75. Case,B.C., Hartley,S., Osuga,M., Jeruzalmi,D. and Hingorani,M.M. (2019) The ATPase mechanism of UvrA2 reveals the distinct roles of proximal and distal ATPase sites in nucleotide excision repair. *Nucleic Acids Res.*, **47**, 4136–4152.
76. Croteau,D.L., DellaVecchia,M.J., Perera,L. and Van Houten,B. (2008) Cooperative damage recognition by UvrA and UvrB: identification of UvrA residues that mediate DNA binding. *DNA Repair (Amst.)*, **7**, 392–404.
77. Kraithong,T., Hartley,S., Jeruzalmi,D. and Pakotiprapha,D. (2021) A peek inside the machines of bacterial nucleotide excision repair. *Int. J. Mol. Sci.*, **22**, 952.
78. Grossman,L. and Thiagalingam,S. (1993) Nucleotide excision repair, a tracking mechanism in search of damage. *J. Biol. Chem.*, **268**, 16871–16874.
79. Hsu,D.S., Kim,S.T., Sun,Q. and Sancar,A. (1995) Structure and function of the UvrB protein. *J. Biol. Chem.*, **270**, 8319–8327.
80. Lin,J.J. and Sancar,A. (1992) (A)BC excinuclease: the Escherichia coli nucleotide excision repair enzyme. *Mol. Microbiol.*, **6**, 2219–2224.
81. Van Houten,B. (1990) Nucleotide excision repair in *Escherichia coli*. *Microbiol. Rev.*, **54**, 18–51.
82. Yoakum,G.H. and Grossman,L. (1981) Identification of *E. coli* UvrC protein. *Nature*, **292**, 171–173.
83. Blanchard,L., Guérin,P., Roche,D., Cruveiller,S., Pignol,D., Vallenet,D., Armengaud,J. and de Groot,A. (2017) Conservation and diversity of the IrrE/DdrO-controlled radiation response in radiation-resistant *Deinococcus* bacteria. *Microbiologyopen*, **6**, e00477.
84. Eugénie,N., Zivanovic,Y., Lelandais,G., Coste,G., Bouthier de la Tour,C., Bentchikou,E., Servant,P. and Confalonieri,F. (2021) Characterization of the radiation desiccation response regulon of the radioresistant bacterium *Deinococcus radiodurans* by integrative genomic analyses. *Cells*, **10**, 2536.
85. Liu,Y., Zhou,J., Omelchenko,M.V., Beliaev,A.S., Venkateswaran,A., Stair,J., Wu,L., Thompson,D.K., Xu,D., Rogozin,I.B. *et al.* (2003) Transcriptome dynamics of *Deinococcus radiodurans* recovering from ionizing radiation. *Proc. Natl. Acad. Sci. U.S.A.*, **100**, 4191–4196
86. Moolenaar,G.F., van Rossum-Fikkert,S., van Kesteren,M. and Goosen,N. (2002) Cho, a second endonuclease involved in *Escherichia coli* nucleotide excision repair. *Proc. Natl. Acad. Sci. U.S.A.*, **99**, 1467–1472.
87. Perera,A.V., Mendenhall,J.B., Courcelle,C.T. and Courcelle,J. (2016) Cho endonuclease functions during DNA interstrand cross-link repair in *Escherichia coli*. *J. Bacteriol.*, **198**, 3099–3108.
88. Timmins,J. and Moe,E. (2016) A decade of biochemical and structural studies of the DNA repair machinery of *Deinococcus radiodurans*. *Comput. Struct. Biotechnol. J.*, **14**, 168–176.